Journal of Catalysis 283 (2011) 10–24

Contents lists available at ScienceDirect

Journal of Catalysis

journal homepage: www.elsevier.com/locate/jcat

Selectivity of chemisorbed oxygen in C–H bond activation and CO oxidation and kinetic consequences for CH_4–O_2 catalysis on Pt and Rh clusters

Ya-Huei (Cathy) Chin [a], Corneliu Buda [b], Matthew Neurock [b,c,*], Enrique Iglesia [a,*]

[a] Department of Chemical and Biomolecular Engineering, University of California, Berkeley, CA 94720, USA
[b] Department of Chemical Engineering, University of Virginia, Charlottesville, VA 22904, USA
[c] Department of Chemistry, University of Virginia, Charlottesville, VA 22904, USA

ARTICLE INFO

Article history:
Received 16 March 2011
Revised 4 June 2011
Accepted 12 June 2011
Available online 12 August 2011

Keywords:
CH_4
Catalytic partial oxidation
Methane combustion
Platinum
Rhodium
CO oxidation
Density functional theory
C–H bond activation
Transition state theory
Oxygen selectivity

ABSTRACT

Rate measurements, density functional theory (DFT) within the framework of transition state theory, and ensemble-averaging methods are used to probe oxygen selectivities, defined as the reaction probability ratios for O* reactions with CO and CH_4, during CH_4–O_2 catalysis on Pt and Rh clusters. CO_2 and H_2O are the predominant products, but small amounts of CO form as chemisorbed oxygen atoms (O*) are depleted from cluster surfaces. Oxygen selectivities, measured using ^{12}CO–$^{13}CH_4$–O_2 reactants, increase with O_2/CO ratio and O* coverage and are much larger than unity at all conditions on Pt clusters. These results suggest that O* reacts much faster with CO than with CH_4, causing any CO that forms and desorbs from metal cluster surfaces to react along the reactor bed with other O* to produce CO_2 at any residence time required for detectable extents of CH_4 conversion. O* selectivities were also calculated by averaging DFT-derived activation barriers for CO and CH_4 oxidation reactions over all distinct surface sites on cubo-octahedral Pt clusters (1.8 nm diameter, 201 Pt atoms) at low O* coverages, which are prevalent at low O_2 pressures during catalysis. CO oxidation involves non-activated molecular CO adsorption as the kinetically relevant step on exposed Pt atoms vicinal of chemisorbed O* atoms (on *–O* site pairs). CH_4 oxidation occurs via kinetically relevant C–H bond activation on *–* site pairs involving oxidative insertion of a Pt atom into one of the C–H bonds in CH_4, forming a three-centered HC_3–Pt–H transition state. C–H bond activation barriers reflect the strength of Pt–CH_3 and Pt–H interactions at the transition state, which correlates, in turn, with the Pt coordination and with CH_3* binding energies. Ensemble-averaged O* selectivities increase linearly with O_2/CO ratios, which define the O* coverages, via a proportionality constant. The proportionality constant is given by the ratio of rate constants for O_2 dissociation and C–H bond activation elementary steps; the values for this constant are much larger than unity and are higher on larger Pt clusters (1.8–33 nm) at all temperatures (573–1273 K) relevant for CH_4–O_2 reactions. The barriers for the kinetically relevant C–H bond dissociation step increase, while those for CO oxidation remain unchanged as the Pt coordination number and cluster size increase, and lead, in turn, to higher O* selectivities on larger Pt clusters. Oxygen selectivities were much larger on Rh than Pt, because the limiting reactants for CO oxidation were completely consumed in ^{12}CO–$^{13}CH_4$–O_2 mixtures, consistent with lower CO/CO_2 ratios measured by varying the residence time and O_2/CH_4 ratio independently in CH_4–O_2 reactions. These mechanistic assessments and theoretical treatments for O* selectivity provide rigorous evidence of low intrinsic limits of the maximum CO yields, thus confirming that direct catalytic partial oxidation of CH_4 to CO (and H_2) does not occur at the molecular scale on Pt and Rh clusters. CO (and H_2) are predominantly formed upon complete O_2 depletion from the sequential reforming steps.

1. Introduction

The direct catalytic partial oxidation (CPOX) of methane is mildly exothermic ($\Delta H^{o}_{reaction} = -35.9$ kJ mol^{-1}) and provides an attractive thermoneutral route to H_2–CO mixtures suitable as reactants in methanol and Fischer–Tropsch syntheses [1,2]. H_2 and CO may form via direct CH_4–O_2 reactions, as proposed based on high CO selectivities ($CO/CO_2 > 90\%$) in short monolith reactors [3,4]. These direct paths seem inconsistent with the fast reactions of H_2 and CO with chemisorbed oxygen atoms (O*) at the conditions required for CH_4 activation. H_2–CO mixtures with direct partial oxidation stoichiometries ($H_2/CO = 2$) can also form (with the same overall reaction enthalpy) via initial CH_4 combustion to CO_2 and H_2O and their subsequent reactions with the remaining CH_4 [5].

* Corresponding authors. Addresses: Department of Chemical Engineering, University of Virginia, Charlottesville, VA 22904, USA (M. Neurock). Department of Chemical and Biomolecular Engineering, University of California, Berkeley, CA 94720, USA. Fax: +1 510 642 4778 (E. Iglesia).
E-mail addresses: mn4n@virginia.edu (M. Neurock), iglesia@berkeley.edu (E. Iglesia).

0021-9517/$ - see front matter © 2011 Elsevier Inc. All rights reserved.
doi:10.1016/j.jcat.2011.06.011

These sequential combustion and reforming reactions can proceed within axial conduction distances in a reactor, thus enabling the thermal coupling of exothermic and endothermic reactions without the direct molecular coupling implied by catalytic partial oxidation. The discrimination between direct and indirect routes to H_2 and CO from CH_4–O_2 reactants is made difficult by the ubiquitous presence of temperature and concentration gradients within packed-beds, monoliths, or catalyst pellets, caused by fast endothermic and exothermic reactions [6–8] and by thermodynamic constraints that corrupt the intended chemical origins and the mechanistic interpretations of measured rates and selectivities [9,10].

Here, we address the persistent controversies regarding the occurrence of direct catalytic partial oxidation on Pt and Rh catalysts by measuring rates and selectivities for CH_4–O_2 reactions under conditions of strict kinetic control. Only trace amounts of CO were detected at any conditions that retained measurable O_2 concentrations in the reactor effluent. The yields of CO reflect the ratios of rate constant for CO and CH_4 reactions with O_2, described here in terms of the relevant elementary steps and their rate and equilibrium constants. These ratios, measured using $^{13}CH_4$–^{12}CO–O_2 mixtures, showed much higher rate constants for ^{12}CO oxidation than for $^{13}CH_4$ oxidation at all O_2 pressures and oxygen surface coverages. These conclusions are consistent with ensemble-averaged ratio of rate constants derived in the framework of transition state theory using DFT-calculated activation barriers of CO and CH_4 oxidation steps on Pt clusters. These experimental and theoretical data indicate that H_2 and CO do not form directly from CH_4–O_2 mixtures because any CO that desorbs from catalyst surfaces would form CO_2 via subsequent oxidation along the catalyst bed at all residence times required for measurable CH_4 conversions. Partial oxidation products (CO and H_2) are exclusively formed from subsequent reactions of CO_2 and H_2O with CH_4 after depletion of the limiting O_2 reactant on Pt and Rh catalysts at CH_4 conversions of practical interest.

2. Experimental and theoretical methods

2.1. Synthesis and characterization of Pt and Rh catalysts

Pt and Rh clusters on γ-Al_2O_3 or SiO_2 were prepared by incipient wetness impregnation with aqueous solutions of hexachloroplatinic acid (H_2PtCl_6, Aldrich, CAS #16941-12-1, 8 wt.% solution) or rhodium(III) nitrate ($Rh(NO_3)_3$, Aldrich, CAS #13139-58-9, 10 wt.% solution), respectively. γ-Al_2O_3 (Sasol, Lot #C1643, 193 $m^2\ g^{-1}$, 0.57 $cm^3\ g^{-1}$ pore volume) was treated in flowing dry air (Praxair, zero grade, 0.8 $cm^3\ g^{-1}\ s^{-1}$) by heating (at 0.083 K s^{-1}) to 998 K or 1123 K (for Pt and Rh catalyst preparation, respectively) and holding for 3 h. X-ray diffractograms of treated Al_2O_3 samples showed the exclusive presence of γ-phase Al_2O_3. SiO_2 (Grace Davison, Grade 62, Lot #995, 280 $m^2\ g^{-1}$) was treated in flowing dry air (Praxair, zero grade, 0.8 $cm^3\ g^{-1}\ s^{-1}$) by heating to 923 K at 0.083 K s^{-1} and holding for 3 h. These supports were impregnated to incipient wetness with the respective metal precursors and treated in ambient air at 383 K for 8 h and in flowing dry air (Praxair, zero grade, 0.8 $cm^3\ g^{-1}\ s^{-1}$) by heating to 998 K (for Pt) or 1123 K (for Rh) at 0.083 K s^{-1} and holding for 3 h. Samples were cooled to ambient temperature and then treated in a flowing H_2/Ar mixture (9% H_2/Ar, Praxair, Certified Standard) by heating to 923 K (0.083 K s^{-1}, 0.8 $cm^3\ g^{-1}\ s^{-1}$) and holding for 2 h and then cooling to 573 K. A He stream (Praxair, UHP grade, 0.8 $cm^3\ g^{-1}\ s^{-1}$) was introduced to the sample at 573 K before cooling to ambient temperature when this stream was then replaced by an O_2/He mixture (0.5% O_2/He, Praxair, Certified Standard, 0.8 $cm^3\ g^{-1}\ s^{-1}$) for 2 h to prevent extensive oxidation of metal clusters upon contact with ambient air.

Pt and Rh dispersions, defined as the atomic ratios of the exposed metal atoms to total metal atoms, were measured from volumetric H_2 uptakes (2–14 kPa, 313 K) (Quantasorb chemisorption analyzer) and determined by extrapolation of strong H_2 adsorption isotherms to zero pressures using a 1:1 $H:M_{surface}$ adsorption stoichiometry [11]. Mean metal cluster diameters were calculated from these dispersion values by assuming hemispherical particles and the bulk densities of Pt (21.45 g cm^{-3}) [12] and Rh (12.41 g cm^{-3}) metals [12].

2.2. Catalytic rate and selectivity measurements

CH_4 conversion turnover rates (per exposed metal atom) and selectivities (on a carbon basis) were measured on a packed-bed of catalyst particles held within a quartz tube (8.1 mm ID) fitted with an axial concentric thermowell that contains a K-type thermocouple. SiO_2 granules (Davison Chemical, Chromatographic Silica Media, CAS #112926-00-8, 280 $m^2\ g^{-1}$, <100 μm) were used as intrapellet diluents for Pt/SiO_2, Pt/Al_2O_3, and Rh/Al_2O_3 catalysts (100–300 SiO_2/catalyst ratios) by mixing, pelletizing, and sieving to retain 100–180 μm agglomerates. These pellets were then mixed loosely with quartz granules (Fluka, #84880, 1000–4700 quartz/catalyst ratios) of similar size and placed in the quartz tube, forming the packed catalyst bed. The catalyst bed (containing 0.15–0.25 mg of Pt/Al_2O_3 or Rh/Al_2O_3) was heated in flowing He (Praxair, UHP grade, 1.67 $cm^3\ s^{-1}$) at 0.083 K s^{-1} to reaction temperatures. Reactant mixtures were prepared using 25% CH_4/He (Matheson Certified Plus Grade), 5% O_2/He (Praxair, Certified Standard), and He (Praxair, UHP grade). Individual flow rates were metered using electronic mass flow controllers (Porter, type 201).

$^{13}CH_4$ (Isotec, 99% ^{13}C purity), 1% ^{12}CO/He (Praxair, Certified Standard), and 5% O_2/He (Praxair, Certified Standard) were used in $^{13}CH_4$–^{12}CO–O_2 isotopic experiments. CH_4, CO, H_2, O_2, and CO_2 molecules were measured by thermal conductivity detection after chromatographic separation (Agilent 3000A Micro GC with channels equipped with 5A and Porapak Q columns). $^{13}CO_2$, $^{12}CO_2$, ^{13}CO, and ^{12}CO concentrations were measured by mass selective detection after similar chromatographic separation (Agilent 5973N MSD and 6890 GC).

2.3. Density functional theory methods

Gradient-corrected plane-wave density functional theory calculations were carried out to determine the optimized structures and energies of reactants, transition states, and products for reactions of adsorbed CH_4 and CO with isolated chemisorbed oxygen atoms (O^*) on a Pt(1 1 1) surface and on different surface sites of cubo-octahedral Pt clusters with 201 atoms (Pt_{201}, N_{total} = 201, 1.8 nm diameter, Scheme 1). The Pt(1 1 1) surface was described using periodic 3 × 3 unit cells comprised of four layers of Pt atoms (9 Pt atoms in each layer) and a 1.5 nm vacuum region to separate the metal surfaces. Pt_{201} cubo-octahedral clusters are low-energy optimized structures and expose eight (1 1 1) (Scheme 1b) and six (1 0 0) (Scheme 1c) edge-shared facets [13]. The (1 1 1) and (1 0 0) terraces on Pt_{201} cluster contain 19 and 9 Pt atoms, respectively; the number of these exposed atoms (N_S), together with the total number of Pt atoms (N_{total} = 201), results in a fractional dispersion (N_S/N_{total}) of 0.61. These surface Pt atoms are denoted as sites 1–4 based on their coordination numbers, and oxygen adsorption sites are denoted as sites I–V, as shown in Scheme 1b and c.

Simulations were carried out by placing the Pt_{201} cluster at the center of a 3 × 3 × 3 nm cubic unit cell and at least 0.8 nm from all cell edges to prevent electronic interactions among clusters. Subsequent simulations with larger 4 × 4 × 4 nm unit cells gave adsorption energies that differ by <2 kJ mol^{-1} from those in the 3 × 3 × 3 nm cell, consistent with the absence of inter-cluster

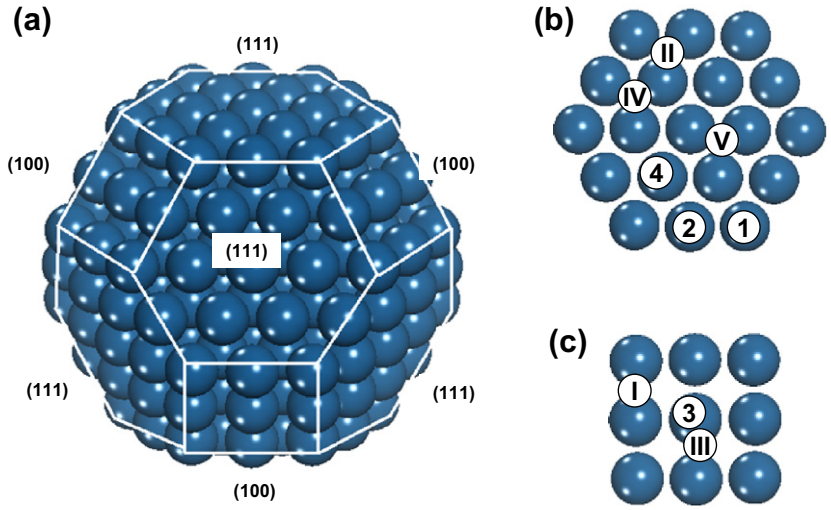

Scheme 1. (a) Model of a cubo-octahedral Pt cluster (1.8 nm cluster size) consists of 201 Pt atoms with: (b) eight (1 1 1) and (c) six (1 0 0) planes. There are four distinct types of surface Pt atom (labeled sites 1–4) depending on their coordination numbers. Oxygen atoms bind on threefold fcc sites (location II, IV, and V) on the (1 1 1) surfaces (b) and on the bridge sites (location I and III) on the (1 0 0) surfaces (c).

interactions. All calculations were carried out using the Perdew Wang 91 (PW91) [14] form of the generalized gradient approximation (GGA) in the Vienna *Ab-initio* Simulation Package (VASP) [15–17]. The wavefunctions were generated using a periodic expansion of plane waves up to a 396 eV kinetic energy cutoff. The interactions between valence and core electrons were described by Vanderbilt ultrasoft pseudopotentials (US-PP) [18]. The electronic state energy of the system was converged to within 9.65×10^{-3} kJ mol^{-1} (10^{-4} eV), whereas the forces on each of the atoms were converged to within 48.2 kJ (mol nm)$^{-1}$ (0.5 eV nm^{-1}). The first Brillouin zone was sampled using $(1 \times 1 \times 1)$ and $(3 \times 3 \times 1)$ Monkhorst–Pack *k*-point meshes for the Pt_{201} clusters and Pt(1 1 1) surfaces, respectively [19]. In the Pt_{201} cluster calculations, all Pt atoms and all adsorbate atoms were fully relaxed. On Pt(1 1 1) surfaces, Pt atoms in the top two layers and adsorbed species were fully relaxed, while Pt atoms in the bottom two layers were held fixed at their bulk distances.

The heat of atomic oxygen adsorption (Q_O, with respect to O_2(g)) is defined here as the negative of the energy for:

$$0.5O_2(g) + Pt \rightarrow O^*{-}Pt \quad (1)$$

in which Pt atoms are present on either Pt_{201} clusters or Pt(1 1 1) surfaces. Q_O is therefore given by the total DFT-optimized energies for a chemisorbed oxygen atom (O^*) on Pt_{201} clusters (or Pt(1 1 1) surfaces), for bare Pt_{201} clusters (or bare Pt(1 1 1) surfaces), and for O_2(g), denoted here as E_{Pt-O}, E_{Pt}, and $E_{O_2(g)}$, respectively:

$$Q_O = -(E_{Pt-O} - E_{Pt} - 0.5E_{O_2(g)}) \quad (2)$$

We assume here that the zero-point energy contributions and any changes in heat capacity between 0 K and 298 K are small compared with overall reaction energies. The heats of non-dissociative adsorption for CO (Q_{CO}) and CH_4 (Q_{CH_4}) are taken as the negative values of the calculated reaction energies for CO and CH_4 molecular adsorption (denoted as $\Delta E_{CO,ads}$ and $\Delta E_{CH_4,ads}$, respectively) on Pt_{201} clusters (or Pt(1 1 1) surfaces):

$$Q_{CO} = -\Delta E_{CO,ads} = -(E_{Pt-CO} - E_{Pt} - E_{CO(g)}) \quad (3)$$

$$Q_{CH_4} = -\Delta E_{CH_4,ads} = -(E_{Pt-CH_4} - E_{Pt} - E_{CH_4(g)}) \quad (4)$$

where E_{Pt-CO} and E_{Pt-CH_4} are the energies for chemisorbed CO and CH_4 on Pt_{201} clusters (or Pt(1 1 1) surfaces), E_{Pt} is the energy of the bare Pt_{201} clusters (or bare Pt(1 1 1) surfaces), and $E_{CO(g)}$ and $E_{CH_4(g)}$ are the energies for the respective optimized gas-phase molecules.

Transition state complexes and reaction barriers for C–H bond dissociation and for CO adsorption and oxidation were calculated using the climbing-image nudged elastic band (CI-NEB) method [20]. Four equally spaced images were chosen between the reactant and product states to represent the reaction coordinate. The forces perpendicular to the reaction coordinate for each of these images were optimized using 50 structural optimization steps to establish the highest energy state along the reaction trajectory. The climbing algorithm was then turned on and used to drive the image that exhibits the highest energy up along the reaction coordinate by maximizing the energy along the tangent to the potential energy surface to within a force of 48.2 kJ (mol nm)$^{-1}$ (0.5 eV nm^{-1}). This is used to isolate a stationary point which is a maximum along the minimum energy path and to calculate the activation energy. Full frequency calculations would be required to ensure that this was the transition state. The significant CPU effort necessary to calculate second derivatives made it prohibitive to carry out full frequency calculations.

2.4. Ensemble-averaged rate constants

The relative rates of CO and CH_4 oxidation were calculated on Pt_{201} clusters (Scheme 1) using statistical and transition state theory methods, DFT estimates of activation barriers on different sites at Pt_{201} cluster surfaces, and measured activation entropies. These reactions can proceed on metal–metal (*–*) and metal–oxygen (*–O^*) site pairs with different barriers depending on the coordination of metal sites or the heat of atomic oxygen adsorption (Eq. (2)); therefore, their barriers were averaged over all possible site pairs on Pt_{201} clusters and taken together with the activation entropies to obtain the ensemble-averaged CO and CH_4 oxidation rate constants. We have examined in detail the reactivity of five distinct oxygen adsorption sites (sites I–V) and four types of Pt sites (sites 1–4), including corner, edge, and terrace locations on (1 1 1) and (1 0 0) surfaces (Scheme 1). We considered clusters with one O^* atom, because such low O^* coverages prevail during CH_4–O_2 reactions at conditions leading to near complete O_2 consumption would favor CO^* desorption before subsequent oxidation to CO_2. Both (1 1 1) and (1 0 0) facets were treated as Langmuirian

surfaces, on which site pairs involved in CO and CH_4 reactions were treated as non-interacting ensembles.

We consider two limiting cases for the distribution of O^* on Pt_{201} clusters: (i) random O^* occupation at all surface Pt sites irrespective of coordination and (ii) site occupancy prescribed by oxygen adsorption thermodynamics (Q_O; Eq. (2)). In the first case, the occupation probability ($P_{j,\text{random}}$) is given by the fraction of O^* atoms of type j among all O^* atoms, where j is a roman numeral from I to V, as shown in Scheme 1. In the second case, $P_{j,\text{weighted}}$ is determined by the number of each type of O^* adsorption site (denoted here as m_j or m_k, where j and k refer to the specific sites I–V in Scheme 1, thus j, k = 1–5 and 1 = I, 2 = II, 3 = III, 4 = IV, 5 = V) and weighted by their heats of atomic oxygen adsorption ($Q_{O,j}$, $Q_{O,k}$):

$$P_{j,\text{weighted}} = \frac{m_j \exp\left(\frac{Q_{O,j}}{RT}\right)}{\sum_{k=1}^{5} m_k \exp\left(\frac{Q_{O,k}}{RT}\right)} \quad (5)$$

3. Results and discussion

3.1. Detection and removal of transport corruptions in measured rates

Rigorous kinetic measurements require the absence of transport restrictions within catalyst pellets and reactors in order to ensure that local temperatures and reactant and product concentrations at active sites reflect those measured in the contacting gas phase. Measured rates and selectivities that do not depend on the extent of catalyst dilution provide the sole unequivocal evidence for strict kinetic control and for the rigorous absence of transport corruptions of measured chemical reaction rates [21,22].

Fig. 1a and b shows CH_4 turnover rates (873 K) at various dilution ratios within the pellets (λ) (100–300 diluent-to-catalyst ratio) or the catalyst bed (χ) (1000–4700 diluent-to-catalyst ratio) at 0.02–0.33 O_2/CH_4 reactant ratios on Pt/Al_2O_3 (0.2 wt.% Pt; 8.5 nm mean Pt cluster diameter). For these O_2/CH_4 values, the O_2/CH_4 ratios determine O^* coverages on cluster surfaces because of the kinetic coupling between irreversible C–H bond and O_2 dissociation steps that form and remove the O^* atoms [23]. Turnover rates reached their highest values (>900 mol CH_4 (g-atom $Pt_{surface}$-s)$^{-1}$, hereinafter denoted as s^{-1}) on Pt surfaces covered partially with chemisorbed oxygen atoms (O^*), which prevail at intermediate O_2/CH_4 ratios (0.07–0.12). These O^* species form *–O^* site pairs with vicinal Pt atoms (*, also denoted as oxygen vacancies on O^* covered surfaces), which activate C–H bonds more effectively than O^*–O^* or *–* site pairs prevalent at larger or smaller O_2/CH_4 ratios, respectively; these *–O^* site pairs lead to the sharp maximum observed in turnover rates at intermediate O_2/CH_4 ratios (Fig. 1a and b) [23]. CO was only detected ($CO/CO_2 < 0.02$) at O_2/CH_4 ratios below 0.04, indicating that CH_4 combustion, instead of partial oxidation, is the predominant catalytic reaction, even at very low O_2/CH_4 ratios (Section 3.2).

Any effects of gradients in temperature and concentration within catalyst pellets and across the film boundaries of gas and solid phases on CH_4 turnover rates (873 K) were ruled out by varying intrapellet dilution ratios (λ; 100–300) at constant bed dilution ratios (χ; 4700). The smallest intrapellet dilution ratios (100) gave higher turnover rates than larger ratios (>200), because of small residual temperature gradients even after such significant dilutions (Fig. 1a). Turnover rates did not depend on intrapellet dilution for λ values above 200, which rendered intrapellet temperature and concentration gradients kinetically undetectable. These results also rule out the gradients across the gas and solid boundaries, because such gradients would lead to rates that depend on the density of active sites within pellets. CH_4 oxidation rates strictly proportional to the number of surface Pt atoms within such pellets and turnover rates independent of intrapellet site densities have rigorously confirmed the removal of these gradients (Fig. 1a).

Bed temperature gradients were probed using physical mixtures of diluent and catalyst particles at bed dilution ratios (χ) of 1000–4700 and constant intraparticle dilution ratios (λ; 200). Bed dilution ratios of 1000 gave higher turnover rates than at higher values ($\chi \geqslant 2000$) at the intermediate O_2/CH_4 ratios (0.06–0.18) that give the highest reaction and heat generation rates (Fig. 1b). Turnover rates became insensitive to bed dilution for χ values above 2000, for which turnover rates no longer depended on the number of sites within the catalyst bed. These extensive dilution levels ($\lambda \geqslant 200$ and $\chi \geqslant 2000$) were required for strict kinetic control and for identical temperatures and concentrations at active sites and in the contacting gas phase; these dilution requirements, which have been seldom (if at all) met in previously reported rate data and correspond to reactor heat loads smaller than 0.35 W cm^{-3} for the dimensions of the reactor and pellets (8.1 mm and 0.180 mm, respectively) used here, are required to eliminate transport artifacts to obtain the rate data and associated mechanistic interpretations.

CH_4–O_2 turnover rates were also measured on Rh/Al_2O_3 (0.2 wt.% Rh; 3.3 nm mean cluster diameter) at similar bed and

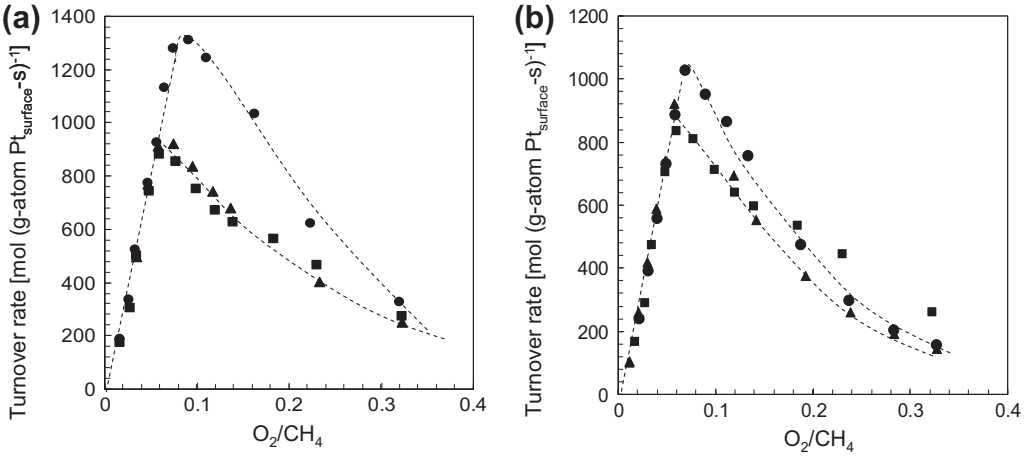

Fig. 1. (a) Effects of intrapellet diluent-to-catalyst ratio (λ) {100 (●), 200 (▲), 300 (■)} on CH_4 turnover rates (per exposed Pt atom; 873 K) on 0.2 wt.% Pt/Al_2O_3 (8.5 nm mean cluster diameter), plotted here as a function of O_2/CH_4 ratio (4700 diluent/catalyst interpellet dilution ratio (χ), 0.15 mg cat., 2.08 cm^3 (STP) s^{-1}, 4.9 kPa CH_4). (b) Effects of interpellet diluent-to-catalyst ratio (χ) {1000 (●), 2000 (▲), 4700 (■)} on CH_4 turnover rates (per exposed Pt atom; 873 K) on 0.2 wt.% Pt/Al_2O_3 (8.5 nm mean cluster diameter), plotted here as a function of O_2/CH_4 ratio (200 diluent/catalyst intrapellet dilution ratio (λ), 0.15 mg cat., 2.08 cm^3 (STP) s^{-1}, 4.9 kPa CH_4).

intrapellet dilutions (λ = 100–300; χ = 1900–2800; Table 1). Turnover rates were smaller on Rh than on Pt at all O_2/CH_4 ratios {maximum rates were ~70 s^{-1} for Rh (Table 1 and Fig. 2) vs. ~900 s^{-1} for Pt (Fig. 1a and b); Section 3.2}; these reaction rates led to a maximum volumetric heat generation rate of 5.4×10^{-2} W cm^{-3}, which was much smaller than that on the Pt catalysts (0.35 W cm^{-3}). Therefore, CH_4–O_2 reactions on Rh are less likely to cause temperature gradients, as confirmed from turnover rates that are independent of the values of λ and χ (Table 1).

These data show that extensive dilutions at the scales of pellets ($\lambda \geqslant 200$; 0.180 mm pellet diameter) and reactor beds ($\chi \geqslant 2000$; 8.1 mm reactor diameter) are required to obtain CH_4–O_2 rate data under conditions of strict kinetic control and to eliminate transport artifacts ubiquitous in these highly exothermic reactions. All rates and selectivities reported herein were measured using these dilution ratios and volumetric heat generation rates much smaller than those causing transport corruptions of chemical rates ($\leqslant$0.35 W cm^{-3}).

3.2. Residence time effects on turnover rates and CO/CO_2 selectivities

Fig. 2a and b show CH_4 turnover rates, CO/CO_2 selectivity ratios, and outlet O_2 pressures as a function of residence time on Pt/Al_2O_3 (0.2 wt.%; 8.5 nm mean cluster diameter) and Rh/Al_2O_3 (0.2 wt.%; 3.3 nm mean cluster diameter) for inlet O_2/CH_4 ratios of 0.125 and 0.13, respectively, which make O_2 the limiting reactant.

On Pt, turnover rates initially increased (from 270 to 370 s^{-1}) as the residence time increased (from 0.4×10^{-4} to 1.2×10^{-4} (g-atom $Pt_{surface}$-s)(mol CH_4)$^{-1}$), but ultimately decreased as O_2 co-reactants were depleted and O_2/CH_4 ratios concurrently decreased. Similar effects were observed when inlet O_2/CH_4 ratios (instead of residence times) were changed while keeping the residence time constant (Fig. 1a and b). These trends were also found on 0.2 wt.% Rh/Al_2O_3 (Fig. 2b). These kinetic effects of O_2/CH_4 ratios reflect changes in the identities of the most abundant surface intermediates (MASI) and of the kinetically relevant steps [23]. As the O^* coverage on Pt clusters decreases with decreasing O_2/CH_4 ratio, the kinetically relevant step shifts from C–H bond activation on oxygen–oxygen (O^*–O^*) site pairs to on metal–oxygen (*–O^*) site pairs, and ultimately to O_2 activation on metal–metal (*–*) site pairs [23]. When O_2 is no longer present, CH_4 reforming becomes the prevalent reaction and C–H bond activation occurs on metal–metal (*–*) site pairs, which forms carbonaceous intermediates that are removed by O^* species derived from H_2O or CO_2 [24].

H_2 was not detected before O_2 depletion on any of the catalysts used, apparently because if formed, it reacted very rapidly with O^* to form H_2O before the reactor exit at all residence times required for practical CH_4 conversions. CO_2 and H_2O were the only products detected even at residence times that led to nearly complete O_2 conversion (1.2×10^{-4} (g-atom $Pt_{surface}$-s)(mol CH_4)$^{-1}$ and 1.4×10^{-3} (g-atom $Rh_{surface}$-s)(mol CH_4)$^{-1}$)). Even at the smallest O_2/CH_4 ratios (<0.04 for Pt; <0.03 for Rh), CO/CO_2 ratios were near CO detection limits (<0.013 for Pt; $\ll$0.005 for Rh) at all residence times that led to detectable O_2 effluent concentrations. These data are consistent with those measured by varying the O_2/CH_4 ratios at a constant residence time (Fig. 1a and b), for which CO was detected (CO/CO_2 < 0.02) only at O_2/CH_4 ratios below 0.04. These effects of residence time and O_2/CH_4 ratio on outlet CO/CO_2 ratios

Table 1
Effects of intraparticle (λ) and interparticle (χ) diluent-to-catalyst ratios on CH_4 turnover rates on 0.2 wt.% Rh/Al_2O_3 (3.3 nm mean cluster diameter) catalyst at 873 K.

Turnover rate (mol CH_4 (g-atom $Rh_{surface}$-s)$^{-1}$)	Heat load (10^{-2} W cm^{-3})	Intraparticle (λ) diluent-to-catalyst ratio	Interparticle (χ) diluent-to-catalyst ratio
65.3	5.4	300	1900
68.1	3.8	300	2800
62.0	3.5	200	2800
71.9	4.1	100	2800

(0.37 mg cat., 0.583 cm^3 (STP) s^{-1}, 0.13 inlet O_2/CH_4 ratio).

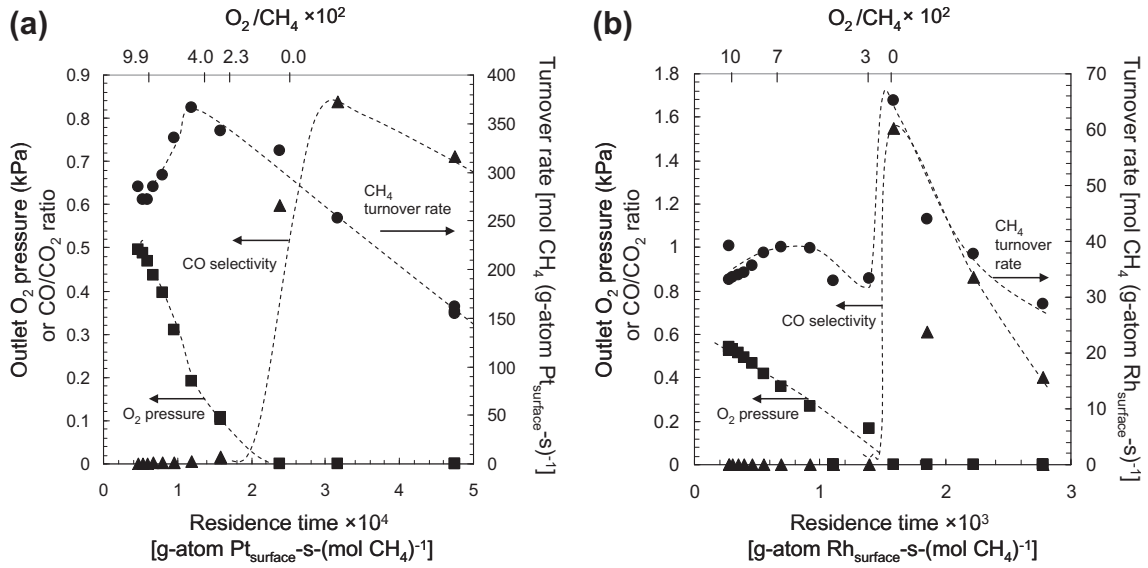

Fig. 2. (a) CH_4 turnover rate (●), outlet O_2 pressure (■), and CO selectivity (▲) during CH_4–O_2 reactions on 0.2 wt.% Pt/Al_2O_3 (8.5 nm mean cluster diameter) as a function of residence time for an inlet O_2/CH_4 feed ratio of 0.13 (873 K, 4.9 kPa CH_4, λ = 200, χ = 4700). O_2/CH_4 ratios at the effluent stream are indicated in the secondary *x*-axis. (b) CH_4 turnover rate (●), outlet O_2 pressure (■), and CO selectivity (▲) during CH_4–O_2 reactions on 0.2 wt.% Rh/Al_2O_3 (3.3 nm average cluster diameter) as a function of residence time for an inlet O_2/CH_4 feed ratio of 0.125 (873 K, 5.0 kPa CH_4, λ = 200, χ = 4700). O_2/CH_4 ratios at the effluent stream are indicated in the secondary *x*-axis.

indicate that CH_4–O_2 reactions form only CO_2 and H_2O at all practical O_2/CH_4 ratios and CH_4 conversion levels.

These results were assessed at shorter residence times than previous studies [3,4] {$\sim 3.6 \times 10^{-5}$ (cm^3 catalyst)-s-(std cm^3 total flow)$^{-1}$ in Fig. 1a and b vs. $\sim 10^{-2}$ (cm^3 monolith volume)-s-(std cm^3 total flow)$^{-1}$ reported in Refs. [3,4]}. Our results contradict the previous findings [3,4] that CO selectively forms at short residence times. These previous conclusions [3,4] were based on data acquired on catalysts wash-coated on monoliths, for which the metal site densities and the volumetric heat generation rates were estimated to be much larger than our samples (~ 135 W cm^{-3} [25] vs. $\leqslant 0.35$ W cm^{-3} used herein). Rate and selectivity data on those samples were influenced strongly by very severe temperature and concentration gradients with a reported temperature difference between the inlet feed and catalyst surfaces exceeding 350 K [3,4]. The very small and typically undetectable CO/CO_2 ratios observed here before O_2 depletion under conditions of strict kinetic control at all residence times and inlet O_2/CH_4 ratios rigorously show that CO and H_2 do not form via direct reactions of CH_4–O_2 mixtures on Pt or Rh catalysts. These results do not rule out CO* desorption but they suggest that CO*, if desorbed unreacted, would re-adsorb and react via subsequent reaction with O* along the catalyst bed at all residence times required for detectable levels of CH_4 conversion. CO (and H_2) molecules form only via secondary reactions of CH_4 with combustion products (CO_2 and H_2O) after O_2 depletion.

The direct formation of CO (or H_2) from CH_4–O_2 reactants requires that CO* (or H*) desorbs from catalyst surfaces before subsequent reactions with O* and that desorbed CO (or H_2) does not re-adsorb and react with O* at reactor residence times required for practical CH_4 conversion. The overall CO yields attainable in CH_4–O_2 reactions depend on the selectivity of O* reactions with CO and CH_4. In what follows, we first address the mechanism for CH_4 and CO reactions with O* and then describe O* selectivities in terms of kinetic and thermodynamic constants for the elementary steps that we propose to account for the kinetic dependence, kinetic isotope effects, and ensemble-averaged rates obtained from transition state and density functional theory. These quantitative and molecular scale interpretations of O* selectivities provide a rigorous assessment on the maximum CO yield attainable from direct CH_4–O_2 reactions (Section 3.7).

3.3. Oxygen selectivities from competitive reactions of ^{12}CO and $^{13}CH_4$ with O_2 on Pt clusters

Here, we consider O* selectivities on Pt clusters essentially uncovered by reactive intermediates, because such surfaces are most likely to desorb CO* (or H*) before subsequent reactions of these species with vicinal O* to form CO_2 (or H_2O). O* selectivities (S_{O^*}) on uncovered Pt surfaces reflect the ratio of reactive collision probabilities of desorbed CO and CH_4 reactant with O*, which are given by the first-order rate constants of CO (k_{O_2-CO}) and CH_4 ($k_{O_2-CH_4}$) oxidation, respectively:

$$S_{O^*} = \frac{k_{O_2-CO}}{k_{O_2-CH_4}} \quad (6)$$

These O* selectivities can be rigorously measured by introducing ^{12}CO into a $^{13}CH_4$–O_2 mixture. The evidence for the low coverage of intermediates on Pt clusters at these low O_2/CH_4 ratios (<0.08 for 8.5 nm Pt clusters) and for the sequence of elementary steps (Scheme 2) involved in CH_4 and CO oxidation via reactions with O* species are consistent with the rate dependencies and kinetic isotope effects reported elsewhere [23]. At these O_2/CH_4 ratios, CH_4 conversion rates are limited by O_2 dissociation steps on uncovered Pt surfaces, as confirmed from rates that are proportional to O_2 pressure and unaffected by either the CH_4 pressure or isotope identity (CH_4/CD_4 kinetic isotope effects = 1.01) and from the small measured activation barriers (<3 kJ mol^{-1}) [23].

$$O_2 + * \xleftrightarrow{K_{O_2}} O_2 * \quad (1)$$

$$O_2 * + * \xrightarrow{k_{O^*}} 2O * \quad (2)$$

$$CH_4 + * \xleftrightarrow{K_{CH_4}} CH_4 * \quad (3)$$

$$CH_4 * + * \underset{\rightarrow}{\overset{k_{[*-*]}}{\rightleftharpoons}} CH_3 * + H * \quad (4)$$

$$CH_4 * + O * \underset{\rightarrow}{\overset{k_{[O^*-*]}}{\rightleftharpoons}} CH_3 * + OH * \quad (5)$$

$$C * + O * \xrightarrow{k_{C^*+O^*}} CO * + * \quad (6)$$

$$* CO \xrightarrow[\leftarrow]{k_{CO\,des}, k_{CO\,ads}} CO + * \quad (7)$$

$$CO * + O * \xrightarrow{k_{CO\,oxi}} CO_2 * + * \quad (8)$$

$$CO_2 * \xleftrightarrow{K_{CO_2}} CO_2 + * \quad (9)$$

$$2H * \xleftrightarrow{K_{H_2}} H_2 + 2 * \quad (10)$$

$$H * + O * \xleftrightarrow{K_{H^*+O^*}} OH * + * \quad (11)$$

$$H * + OH * \xleftrightarrow{K_{H^*+OH^*}} H_2O * + * \quad (12)$$

$$H_2O * \xleftrightarrow{K_{H_2O}} H_2O + * \quad (13)$$

$$CH_x *_S + O *_W \xrightarrow{k_{CH^*}} \quad (14)$$

Scheme 2. A proposed sequence of elementary steps for CH_4–O_2 reactions on Pt clusters uncovered of chemisorbed oxygen atoms. → and ↔ denote irreversible and quasi-equilibrated steps, respectively. k is the rate coefficient and K is the equilibrium constant for the respective elementary step.

O_2 chemisorbs molecularly as O_2* on unoccupied Pt sites (*, Step 1, refer to Scheme 2 herein for the identity of elementary steps) [26] and subsequently dissociates on vicinal * sites to form O* (Step 2). CH_4 adsorbs weakly on vacant sites (*, Step 3) and then reacts with vicinal * species to form CH_3* and H* (Step 4). CH_4* can also react with vicinal O* species to form CH_3* and OH* (Step 5). In either case, the CH_3* subsequently decomposes via successive H-abstractions and O* insertions (Step 6) to form CO*. CO* can desorb (Step 7) or react with another O* to form CO_2 (Steps 8 and 9). Similarly, H* can recombine with another H* to form H_2 (Step 10) or react with O* and then H* (or OH*) to form H_2O (Steps 11–13). These steps also include the possible readsorption of CO and H_2 (reverse of Steps 7 and 10) to re-form CO* and H*, which can react with O* to form CO_2 and H_2O and complete a combustion turnover.

CO oxidation turnover rates are proportional to O_2 pressure and unaffected by CO pressure [23], consistent with kinetically relevant O_2 dissociation steps on bare Pt clusters. In fact, CH_4 [23], C_2H_6 [27], and CO [23] oxidation rates on uncovered Pt clusters were all independent of the identity, concentration, or reactivity of the reductant and limited solely by O_2 activation steps. Thus, these rates are related to the O_2 consumption rates (r_{O_2}) by their respective reaction stoichiometries. O_2 consumption rates are proportional to O_2 pressures with an effective rate constant given by the product of O_2 adsorption equilibrium constant (K_{O_2}) and O_2* dissociation rate constant (k_{O^*}), as defined in Steps 1 and 2, respectively, and derived elsewhere [23,27]. O_2 consumption rates were identical (Table 2; Entries 1–2, 0.2 wt.% Pt/SiO_2, 33 nm mean cluster diameter), and CO (r_{CO}) and CH_4 (r_{CH_4}) turnover rates for CO–O_2 and CH_4–O_2 reactants are related to each other and to the O_2 consumption rates by reaction stoichiometry:

Table 2
O_2 turnover rates during $^{13}CH_4$–^{12}CO–O_2, $^{12}CH_4$–O_2, and ^{12}CO–O_2 reactions and ratios of O_2 turnover rates in $^{13}CH_4$–^{12}CO–O_2 and CO–O_2 mixtures (β, Eq. (17)) on supported Pt clusters of 1.8 nm and 33 nm mean cluster diameters (0.2 wt.% Pt supported on Al_2O_3 and SiO_2, respectively) at 873 K.

Entry	Pt cluster size (nm)	Reactant mixture	O_2 pressure (kPa)	$\frac{(O_2)}{(CO)}$	$\frac{(O_2)}{(CH_4)}$	O_2 turnover rates (mol O_2 (g-atom $Pt_{surface}$-s)$^{-1}$)	β
1	33	$^{12}CH_4$–O_2	0.036	–	0.022 [52]	500.1	–
2	33	^{12}CO–O_2	0.036	0.23	–	512.4	–
3	33	$^{13}CH_4$–^{12}CO–O_2	0.036	0.23	0.022	496.0	0.99
4	1.8	^{12}CO–O_2	0.009	0.024	–	9.0	–
5	1.8	$^{13}CH_4$–^{12}CO–O_2	0.009	0.024	0.008	7.5	0.83
6	1.8	$^{13}CH_4$–^{12}CO–O_2	0.009	0.024	0.0033	7.1	0.79

(λ = 200, χ = 4700, 0.15 mg cat., 2.08 cm^3 (STP) s^{-1}).

$$r_{O_2} = 2r_{CH_4} = 0.5r_{CO} = K_{O_2}k_{O^*}(O_2) \quad (7)$$

In CH_4–CO–O_2 mixtures, O_2 consumption rates are also limited by O_2 activation and are given by the combined rates of O_2 reactions with CH_4 and CO (and H_2) weighed by their respective conversion stoichiometries. O_2 consumption rates in CH_4–CO–O_2 mixtures (Table 2, Entry 3) are similar to those measured with CO–O_2 or CH_4–O_2 mixtures (Entries 1–2) for a given O_2 pressure, because CH_4 and CO oxidation share a common kinetically relevant O_2 dissociation step. O_2 consumption rates in CH_4–CO–O_2 mixtures are given by:

$$r_{O_2} = 2\nu_1 r_{CH_4,1} + 0.5\nu_2 r_{CH_4,2} + 0.5r_{CO} + 0.5r_{H_2} \quad (8)$$

in which $r_{CH_4,1}$ and $r_{CH_4,2}$ are the rates of CH_4 conversion to CO_2 and H_2O and to CO and H_2, respectively, r_{H_2} is the rate of sequential H_2 reactions with O_2, and ν_1 and ν_2 are the selectivity ratios. Although CO forms only in trace concentrations from CH_4–O_2 reactants before O_2 depletion (Section 3.2), CO may form more readily from CH_4 when additional CO is added to the CH_4–O_2 reactants, because CO effectively scavenges O* (as shown later in this section) and decreases the O* coverages. At the low O* coverages prevalent in CH_4–CO–O_2 mixtures, rates of initial C–H bond activation are largely unaffected by O* concentrations and thus remain similar to those in CH_4–O_2 mixtures, because O* atoms are not involved in the kinetically relevant C–H bond activation step (Sections 3.3 and 3.5–3.6). The sequential oxidation of the CO* intermediates formed from CH_4, however, becomes much less effective at the low O* coverages, because this step requires an O* atom vicinal to the CO* (Section 3.6). This decrease in CO* oxidation rates leads to incomplete CH_4 oxidation and thus to CO formation from CH_4 in CH_4–CO–O_2 mixtures. The first-order rate constants for O_2 reactions with CH_4 ($k_{O_2-CH_4}$) and CO (k_{O_2-CO}) on bare Pt surfaces are given by their turnover rates divided by the respective reactant pressure:

$$k_{O_2-CH_4} = \frac{2\nu_1 r_{CH_4,1} + 0.5\nu_2 r_{CH_4,2} + 0.5r_{H_2}}{(CH_4)} \quad (9)$$

$$k_{O_2-CO} = \frac{0.5r_{CO}}{(CO)} \quad (10)$$

Their ratios give the O* selectivities (S_{O^*}) upon substitution into Eq. (6).

O* selectivities were measured from $^{12}CO_2$, $^{13}CO_2$, and ^{13}CO formation rates using $^{13}CH_4$–^{12}CO–O_2 mixtures (O_2/CO = 0.02–0.23; O_2/CH_4 = 0.0027–0.017) on Pt clusters (1.8 nm and 33 nm mean diameters, 0.2 wt.% Pt) at 873 K. O_2 turnover rates (also the total CO and CH_4 rates) were proportional to O_2 pressure, consistent with O_2 dissociation on essentially uncovered Pt cluster surfaces as the kinetically relevant step during catalysis. O* selectivities (Eq. (6)) are shown in Fig. 3 as a function of O_2/CO inlet ratios. These selectivities were much greater than unity (10–60), indicating that O* atoms react preferentially with CO* instead of CH_4 on Pt clusters. O* selectivities increased with O_2/CO ratios on both large and small Pt clusters, but were higher on larger Pt clusters. The mechanistic origins of these size effects are discussed in Section 3.4.

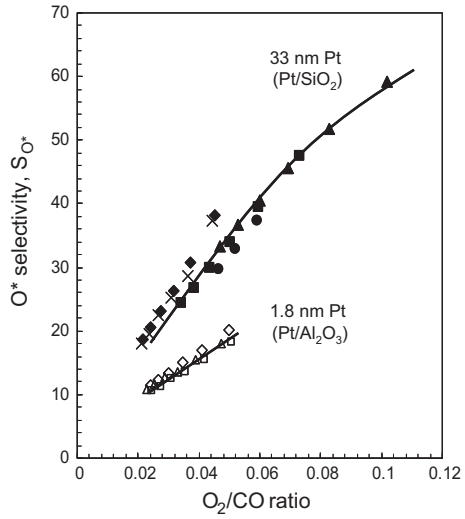

Fig. 3. O* selectivity (S_{O^*}, 873 K) during competitive $^{13}CH_4$–^{12}CO oxidation reactions on 1.8 nm and 33 nm Pt clusters as a function of O_2/CO ratio (0.3 mg 0.2 wt.% Pt/Al_2O_3 or Pt/SiO_2, respectively; 1.2 kPa (△), 2.0 kPa (□, ×), 2.8 kPa (◇, ♦, ▲, ■), and 4.2 kPa (●) CH_4; 0.008 kPa (♦, ×), 0.009 kPa (□, ◇, △), 0.013 kPa (■), and 0.017 kPa (▲, ●) O_2, 2.08 cm^3 s^{-1}, λ = 200, χ = 4700).

O* coverages reflect the kinetic coupling between steps that scavenge O* using CO and CH_4 and the step that forms O* via O_2 dissociation. The fractional O* coverages during steady-state $^{13}CH_4$–^{12}CO–O_2 reactions, denoted as $[(O^*)/(L)]_{CO-CH_4-O_2}$ where L is the total number of exposed Pt sites, are given by a pseudo steady-state treatment for O* intermediates with unoccupied sites (*) as the most abundant surface intermediates (MASI). This treatment, together with the assumption that the concentration of * equals L, leads the O* coverages to become proportional to O_2/CO ratios with a coefficient that contains the equilibrium constant for O_2 adsorption (K_{O_2}) and the rate constants for O_2^* dissociation (k_{O^*}) and CO adsorption ($k_{CO\ ads}$) (defined in Scheme 2), as derived in Appendix (Supplementary material):

$$\left(\frac{(O^*)}{(L)}\right)_{CO-CH_4-O_2} = \frac{2K_{O_2}k_{O^*}}{k_{CO\ ads}}\left(\frac{O_2}{CO}\right) \quad (11)$$

The kinetic relevance of the molecular CO adsorption step in CO oxidation reactions and the presence of its rate constant ($k_{CO\ ads}$) in Eq. (11) are shown in Section 3.6. The linear relationships between O* coverage and O_2/CO ratios (Eq. (11)) and between O* selectivity and O_2/CO ratios (for ratios below 0.06 on 33 nm Pt clusters, Fig. 3) provide evidence for a concomitant relationship between the O* coverage and selectivity; this relation indicates, in turn, that reactive collision probabilities for CO oxidation (the numerator

term in Eq. (6)) relative to those of CH_4 increase with increasing O^* coverage.

A Langmuir treatment for CO oxidation reactions requires immobile O^* atoms adjacent to CO. The observed linear increase in O^* selectivity with increasing O_2/CO ratio, which defines the O^* coverage (Eq. (11)), for O_2/CO ratios below 0.06 (on 33 nm Pt clusters, Fig. 3) indicates that the reactive CH_4 collision probabilities appeared in the denominator of the O^* selectivity expression (Eq. (6)) are insensitive to O^* coverages. This suggests that kinetically relevant C–H bond activation occurs on exposed metal atom site pairs (*–*) with O^* atoms involved only in latter steps that remove the carbonaceous CH_x^* (x = 1–3) and H^* produced from the C–H bond activation steps. These kinetic treatments, together with the assumption that the selectivity ratios for CH_4 to form CO_2 and CO in CH_4–CO–O_2 mixtures (ν_1 and ν_2) are equal [28], lead to the selectivity expression:

$$S_{O^*} = \frac{k_{CO ads}}{7k_{[^*-^*]}K_{CH_4}}\left(\frac{[O^*]}{[L]}\right) = \frac{k_{O^*}K_{O_2}}{3.5k_{[^*-^*]}K_{CH_4}}\left(\frac{O_2}{CO}\right) \quad (12)$$

which depends on the CH_4 (K_{CH_4}) and O_2 (K_{O_2}) adsorption equilibrium constants, the C–H bond activation ($k_{[^*-^*]}$) and O_2 dissociation (k_{O^*}) rate constants, as defined in Scheme 2, and O_2/CO ratios. This expression was derived by substituting Eq. (11) into Eqs. (6), (9), and (10), the details of which are shown in Appendix (Supplementary material). The linear increase in S_{O^*} with O_2/CO ratio (Eq. (12)) was confirmed from the selectivity data measured on 33 nm Pt clusters for O_2/CO ratios below 0.06 (Fig. 3). In contrast, the alternate route in which kinetically relevant C–H bond activation occurs on *–O^* site pairs (Step 5) would cause the S_{O^*} values to be unaffected by O_2/CO ratios because these ratios determine the O^* concentrations required for both the CO and CH_4 oxidation steps and affect both rates to the same extent (derivation in Appendix (Supplementary material)):

$$S_{O^*} = \frac{k_{CO\ ads}}{7k_{[O^*-^*]}K_{CH_4}} \quad (13)$$

The coordination of exposed Pt atoms influences O^* selectivities because of its consequences for O_2 dissociation and C–H bond activation rate constants. O_2 dissociation is non-activated and its rate constant ($k_{O^*}K_{O_2}$, Eq. (7)) is insensitive to Pt coordination [23]. Rate constants for C–H bond activation on *–* site pairs ($k_{[^*-^*]}K_{CH_4}$), however, depend strongly on Pt coordination [24]. The rate constant for C–H bond activation increases as surface atoms become more coordinatively unsaturated with decreasing cluster size (Pt [24], Rh [29], Ru [30], Pd [31]), consistent with the lower C–H bond activation barriers resulting from more effective stabilization of reaction products (CH_3^* and H^*) on the corner and edge sites prevalent on small clusters (as described in Section 3.5). These effects of surface Pt coordination on C–H bond activation rate constants are responsible for the lower O^* selectivities observed on smaller clusters at all O_2/CO ratios (0.02–0.05; Fig. 3).

S_{O^*} values become smaller than expected from the predicted linear trend with O_2/CO ratios (Eq. (12)) at higher O_2/CO ratios (>0.06) on the 33 nm Pt clusters and for the entire range of O_2/CO ratios (0.02–0.05) on the 1.8 nm clusters. The deviation in S_{O^*} is a result of an apparent increase in its denominator, the reactive collision probabilities of CH_4 with O^* ($k_{O_2-CH_4}$, Eq. (9)), with increasing O_2/CO ratio and O^* coverage. In the next section, we show that the $k_{O_2-CH_4}$ increase is resulted from the removal of CH_x^* species chemisorbed on coordinatively unsaturated corner and edge sites of Pt clusters via reactions with O^* to form CO or CO_2. As a consequence, these under-coordinated surface atoms that are more reactive than terrace sites [24] become accessible for C–H bond activation and participate in catalytic turnovers (Step 4), thus increasing the overall reactive collision probabilities of CH_4 with O^* ($k_{O_2-CH_4}$, Eq. (9)) and decreasing the O^* selectivities.

3.4. Site occupation by carbonaceous intermediates produced from the initial C–H bond activation steps and their effects on oxygen selectivities

Next, we examine the dependence of reactive collision probabilities for $^{13}CH_4$ reactions (also the effective rate constants, $k_{O_2-CH_4}$, Eq. (9)) on $^{13}CH_4$ pressure and show that the CH_x^* species, produced from the C–H bond activation steps, bind reversibly on a portion of the Pt sites at the low O^* coverages prevalent in $^{13}CH_4$–^{12}CO–O_2 mixtures. We propose that the binding of CH_x^* on these sites at low O_2/CO ratios and their gradual removal as the O_2/CO ratio increases cause the deviation in O^* selectivity from the predicted linear trend with the O_2/CO ratio (Eq. (12)) in Fig. 3. We consider Pt atoms with high coordination (denoted as $^*_W$) to remain accessible for the kinetically relevant initial C–H bond activation in CH_4 (Step 4). On these sites, elementary steps for the sequential C–H bond dissociation and CH_x^* (x = 1–3) oxidation are kinetically irrelevant. In contrast, coordinatively unsaturated Pt atoms (denoted as $^*_S$) bind the carbonaceous intermediates produced from the initial C–H bond activation steps ($CH_x^*{}_S$) strongly. On these coordinatively unsaturated $^*_S$ sites, initial C–H bond activation becomes kinetically irrelevant and the removal of $CH_x^*{}_S$ species via oxidation by vicinal reactive oxygen intermediates (Step 14, elementary rate constant k_{CH^*}, Scheme 2) limits the CH_4 turnover rates. The rates of $CH_x^*{}_S$ reactions with O^* increase as O^* coverage (set by O_2/CO ratio) increases. The coordinatively unsaturated $^*_S$ sites are surrounded predominantly by the $^*_W$ sites, thus CH_4 turnover rates ($r_{CH_4,S}$) on these $^*_S$ sites are given by:

$$r_{CH_4,S} = k_{CH^*}(CH_x^*{}_S)\frac{(O^*{}_W)}{L} \quad (14)$$

where $O^*{}_W$ refers to the chemisorbed oxygen atom binds on the $^*_W$ site vicinal of the $^*_S$ site. A pseudo steady-state approximation of the carbonaceous intermediates ($CH_x^*{}_S$) and the assumption of $O^*{}_S$ as minority surface species (relative to $^*_S$ and $CH_x^*{}_S$) give the first-order CH_4 reaction rate constant for the $^*_S$ sites ($k_{CH_4,S}$), as derived in Appendix (Supplementary material):

$$k_{CH_4,S} = \frac{r_{CH_4,S}}{(CH_4)} = \frac{k_{[^*-^*],S}}{\left(1+\frac{k_{[^*-^*],S}}{k_{CH^*}}(CH_4)\frac{k_{CO\ ads}}{2K_{O_2}k_{O^*}}\left(\frac{CO}{O_2}\right)\right)} \quad (15)$$

where $k_{[^*-^*],S}$ is the elementary rate constant for the initial C–H bond activation on the $^*_S$–$^*_W$ site pairs (Step 4, Scheme 2). The overall first-order CH_4 reaction rate constant (k_{CH_4}, related to $k_{O_2-CH_4}$ via the reaction stoichiometry) is simply the sum of the respective rate constants for $^*_S$ ($k_{CH_4,S}$) and $^*_W$ ($k_{CH_4,W}$) sites, weighted by the relative site abundance, which is given here in terms of the fraction of surface atoms acting as $^*_W$ sites (Γ):

$$k_{CH_4} = \Gamma k_{CH_4,W} + (1-\Gamma)k_{CH_4,S} = \Gamma k_{[^*-^*],W} + (1-\Gamma)\frac{k_{[^*-^*],S}}{\left(1+\frac{k_{[^*-^*],S}}{k_{CH^*}}(CH_4)\frac{k_{CO\ ads}}{2K_{O_2}k_{O^*}}\left(\frac{CO}{O_2}\right)\right)} \quad (16)$$

This equation is used to describe the rate data in Fig. 4, which shows the effective rate constants for $^{13}CH_4$ reactions ($k_{O_2-CH_4}$, Eq. (9)) on a 0.2 wt.% Pt/Al_2O_3 catalyst (1.8 nm mean cluster diameter) as a function of O_2/CO ratio and different $^{13}CH_4$ pressures (1.2–2.8 kPa) in $^{13}CH_4$–^{12}CO–O_2 mixtures at 873 K. The effective rate constants for $^{13}CH_4$ reactions increased slightly with increasing O_2/CO ratio (which determines the O^* coverage; Eq. (11)) and were larger at 1.2 kPa $^{13}CH_4$ than at 2.0 kPa and 2.8 kPa $^{13}CH_4$ pressures for each O_2/CO ratio. A non-linear regression of these data using Eq. (16)

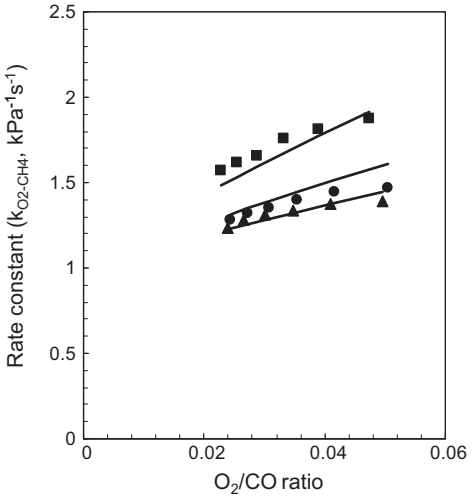

Fig. 4. Effective rate constants (also the reactive collision probabilities) for $^{13}CH_4$ oxidation reactions ($k_{O_2-CH_4}$, Eq. (9), 873 K) in $^{13}CH_4$–^{12}CO–O_2 mixtures as a function of O_2/CO ratio on 0.2 wt.% Pt/Al_2O_3 (1.8 nm mean Pt cluster diameter); the lines are derived from regression of rate data with Eq. (16) (0.3 mg cat.; 1.2 kPa (■), 2.0 kPa (●), and 2.8 kPa (▲) CH_4, 0.0093 kPa (■, ●, ▲) O_2; 2.08 cm^3 s^{-1}, $\lambda = 200$, $\chi = 4700$).

with minimization of residuals and steepest descent algorithms for parameter estimations give the predicted reactive $^{13}CH_4$ collision probabilities, which are plotted together with the measured values in Fig. 4, and the derived kinetic parameters ($\Gamma k_{[*-*],W}$, $(1-\Gamma)k_{[*-*],S}$, $k_{[*-*],S}k_{CO\ ads}(2k_{CH^*}K_{O_2}k_{O^*})^{-1}$) in Table A.1 in Appendix (Supplementary material). Eq. (16) accurately describes the effects of CH_4 pressure. As the oxygen coverage (O^*_W, set by O_2/CO ratio) increases, the $CH_x{}^*{}_S$ coverage decreases and $^*{}_S$ sites become available for catalytic turnovers. The $^*{}_S$ sites are more reactive than the $^*{}_W$ sites for the initial C–H bond activation because of their lower coordinations and concomitantly stronger binding to $CH_3{}^*$ (Section 3.5), leading to higher first-order CH_4 reaction rate constant (k_{CH_4}, Eq. (16)) and to lower O^* selectivities than the predicted linear trend according to Eq. (12) (Fig. 3) at higher oxygen coverages.

The total number of unoccupied sites is smaller during reactions in $^{13}CH_4$–^{12}CO–O_2 than in CO–O_2 mixtures, because $CH_x{}^*$ species are not present during CO–O_2 reactions. O_2 turnover rates in $^{13}CH_4$–^{12}CO–O_2 ($r_{O_2,{}^{13}CH_4-{}^{12}CO-O_2}$) and CO–$O_2$ ($r_{O_2,CO-O_2}$) mixtures are both limited by O_2 dissociation. Their ratio (β) reflects the fraction of exposed Pt atoms that are not covered by $CH_x{}^*$ during $^{13}CH_4$–^{12}CO–O_2 reactions on which the O_2 predominantly reacts with CO:

$$\beta = \frac{r_{O_2,{}^{13}CH_4-{}^{12}CO-O_2}}{r_{O_2,CO-O_2}} \approx \frac{K_{O_2}k_{O^*}(O_2)[(^*)-(CH_x{}^*)]^2}{K_{O_2}k_{O^*}(O_2)(^*)^2} \approx \frac{[(^*)-(CH_x{}^*)]^2}{(L)^2} \quad (17)$$

where L is the total number of exposed Pt atoms. The β values were 0.83 and 0.79 for CH_4 pressures of 1.13 and 2.73 kPa (O_2/CH_4 = 0.008 and 0.0033), respectively, at an O_2/CO ratio of 0.024 on the smaller Pt clusters (1.8 nm mean diameter; Table 2, Entries 5–6). In contrast, the β values are identical within experimental accuracy on the larger Pt clusters (33 nm; $\beta > 0.99$, O_2/CH_4 = 0.022, Table 2, Entry 3) and at a higher O_2/CO ratio (0.23), suggesting that almost all exposed Pt atoms are uncovered by $CH_x{}^*$ species produced from the C–H bond activation steps in $^{13}CH_4$–^{12}CO–O_2 mixtures under those conditions.

3.5. Theoretical assessment of the initial C–H bond dissociation in CH_4 on metal atom site pairs of Pt_{201} clusters

Density functional theory calculations were carried out to determine reaction and activation energies for the initial C–H bond activation of CH_4 over the various Pt sites on model Pt_{201} cubo-octahedral cluster surfaces (1.8 nm diameter, refers to Scheme 1 herein), previously examined on single crystal extended surfaces [32–34]. The structure of the bare Pt_{201} cluster was fully optimized, resulting in an average Pt–Pt distance within the inner core of the cluster (0.282 nm) similar to the value reported for bulk Pt (0.277 nm [35]). The Pt–Pt bond lengths at the corner and edge sites were slightly shorter (0.272 nm) as a result of the lower coordination numbers of these sites (CN_{corner} = 6 and CN_{edge} = 7 for sites 1 and 2, respectively) relative to those of the terrace sites ($CN_{100,terrace}$ = 8 and $CN_{111,terrace}$ = 9 for sites 3 and 4, respectively), which leads to stronger Pt–Pt bonds and to a slight reconstruction at these sites, as also observed experimentally [36]. This bond contraction becomes even more evident on smaller clusters (55 atoms) than on larger clusters, as observed for Pt, Rh, and Pd clusters, because of larger fractions of coordinatively unsaturated atoms residing on the corner and edge sites [37]. The bond contraction at these sites partially compensates for their lower degrees of coordinative saturation and lowers the overall surface free energy. These effects and their catalytic consequences cannot be appropriately captured in periodic calculations on extended and ordered single crystal surfaces because relaxation and reconstruction on such surfaces are constrained by actual structural differences between planar and curved surfaces as well as the computational limitations imposed by periodic cell boundaries. Clusters that are large enough (>100 atoms) such as the Pt_{201} capture the various sites (e.g., terrace, corner, edge, Scheme 1) of working catalytic particles and therefore provide a more reliable theoretical representation than extended flat or stepped surfaces, thus allowing for the systematic studies of the coordination and cluster size effects on catalytic rates.

CH_4 activation on the Pt_{201} cluster proceeds by the initial adsorption of CH_4 (Step 3) on a Pt site, which can be one of the four different Pt sites identified in Scheme 1. The adsorption energy for $CH_4{}^*$ precursors (3 kJ mol^{-1}) from the gradient-corrected exchange–correlation functionals in plane-wave DFT (e.g., PW91) is underpredicted because these functionals do not accurately capture weak attractive van der Waal interactions [38,39]. On both the (1 1 1) and (1 0 0) facets, the dissociation of one of the C–H bonds in $CH_4{}^*$ (Step 4) occurs via an oxidative insertion of the Pt atom into the C–H bond (Fig. A.1b), followed by the transfer of the resulting H to a vicinal Pt–Pt bridge site (Fig. A.1c). The metal site pair (*–*) discussed herein refers to the specific sites where the $CH_3{}^*$ and H^* products reside rather than the total number of Pt atoms involved in the C–H bond dissociation step. Alternatively, the C–H bond dissociation step can proceed on a metal–oxygen site pair via a concerted step involving the oxidative insertion of a Pt atom into the C–H bond and a hydrogen abstraction by a vicinal O^* (Step 5, Fig. A.2), which will be discussed in Section 3.6. The structures of reactant, transition, and product states for the CH_4 activation at each of the different *–* and *–O^* site pairs (Steps 4 and 5, respectively) on the Pt_{201} cluster are given in Figs. A.1 and A.2 and Tables A.2 and A.3 in Appendix (Supplementary material). The reaction energy diagrams and the structures of the intermediates and transition states for the two distinct CH_4 activation paths on *–* and *–O^* site pairs, respectively, are summarized in Fig. 5a.

C–H bond activation on the various *–* site pairs on (1 1 1) and (1 0 0) facets of the Pt_{201} cluster proceeds via mechanistically similar steps in which one of the Pt atoms undergoes oxidative addition into the C–H bond. Here, we first discuss the specific details of this step by using a representative case in which the site pairs consist of two terrace Pt atoms on the (1 1 1) facet (site 4, Scheme

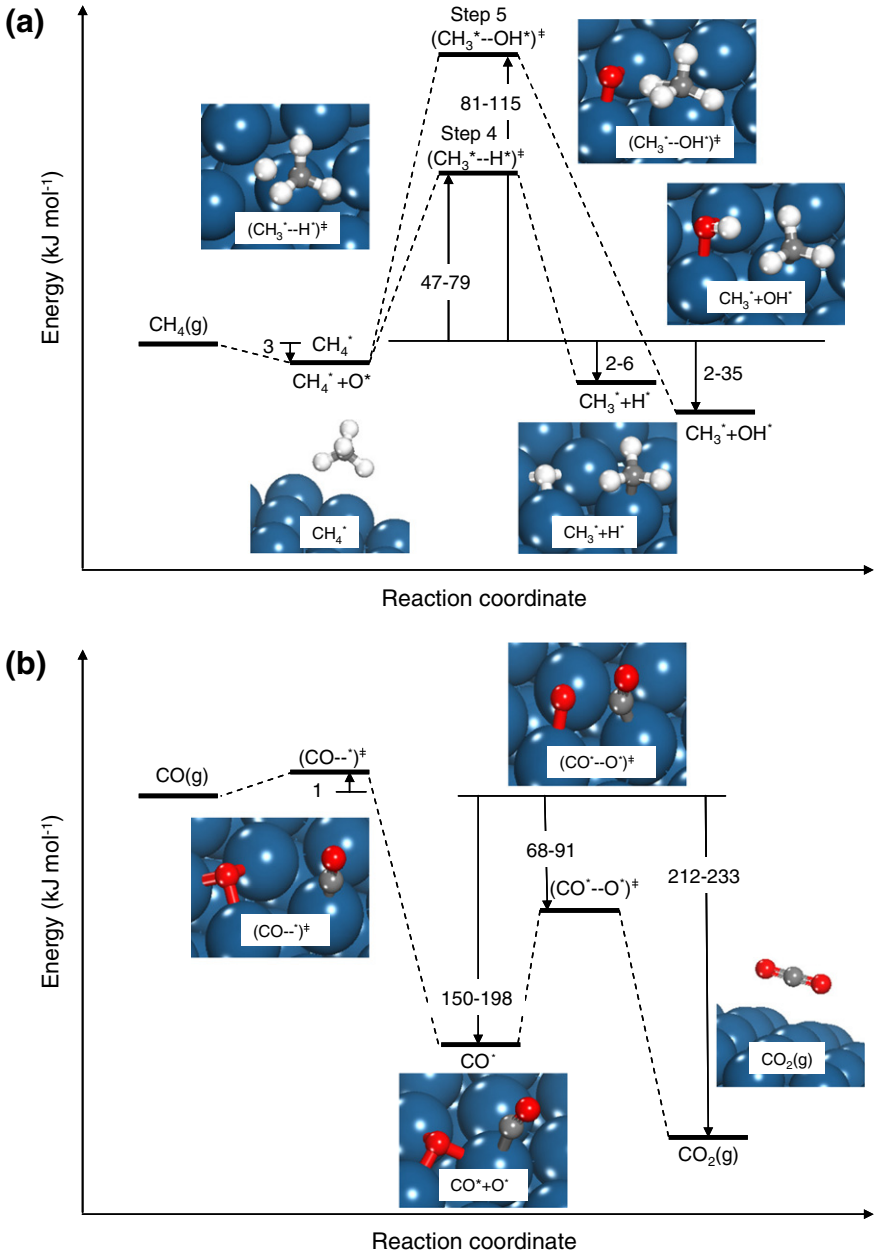

Fig. 5. (a) Reaction energy diagram for initial C–H bond dissociation of CH_4 on the various Pt metal–metal (*–*) (Step 4, Scheme 2) and metal–oxygen (*–O*) site pairs (Step 5, Scheme 2) on Pt_{201} clusters. The energy ranges of intermediates, transition states, and products are given with respect to the reactant energy. (b) Reaction energy diagram for CO oxidation reaction on the various Pt metal–oxygen (*–O*) site pairs on Pt_{201} clusters. The energy ranges of intermediates, transition states, and products are given with respect to the reactant energy. See Appendix (Supplementary material) for the structural details of these steps.

1b) and then the connections between the barriers for this step and the coordination numbers of the different Pt sites on the cluster. The oxidative insertion of Pt into the C–H bond proceeds by the direct interaction of an exposed Pt atom with the C–H bond. This interaction weakens the C–H bond thus resulting in its elongation from 0.109 nm in the CH_4(g) to 0.152 nm in the transition state. The Pt atom (labeled Pt1 in Fig. A.1b) interacts with both the C (0.222 nm) and H (0.162 nm) atoms to form a three-centered carbon–metal–hydrogen $(H_3C^*–H^*)^‡$ activated complex, similar to that involved in C–H bond activation by organometallic complexes [40]. The H–Pt distances between the H-atom and the two vicinal Pt sites (labeled Pt2 and Pt3 in Fig. A.1b) in the transition state are 0.245 nm and 0.261 nm, respectively. These distances are much longer than the Pt–H bond lengths in the product state of 0.174 nm and 0.178 nm (Fig. A.1c), indicating that the vicinal Pt sites do not assist the C–H bond activation steps, but instead promote the H transfer later along the reaction coordinate. The calculated transition state for the C–H bond activation is rather late along the reaction coordinate as there is a significant stretch in the C–H bond (>0.4 nm) and direct occupation of the σ^* C–H bonding state with electron density as was suggested previously for alkane activation over transition metal surfaces [41,42]. The transition state structure suggests strong interactions between the Pt atom that carries out the oxidative insertion step and both the C and H atoms. These interactions indicate the formation of an immobilized $(H_3C^*–H^*)^‡$ transition state complex from a gas-phase CH_4 molecule with a significant loss in entropy. The C–H bond activation step is completed by transferring the H-atom in the C–H bond to a vicinal Pt–Pt bridge site to form the CH_3^* and H^* products. In contrast to Pt(1 1 1) surfaces, C–H bond dissocia-

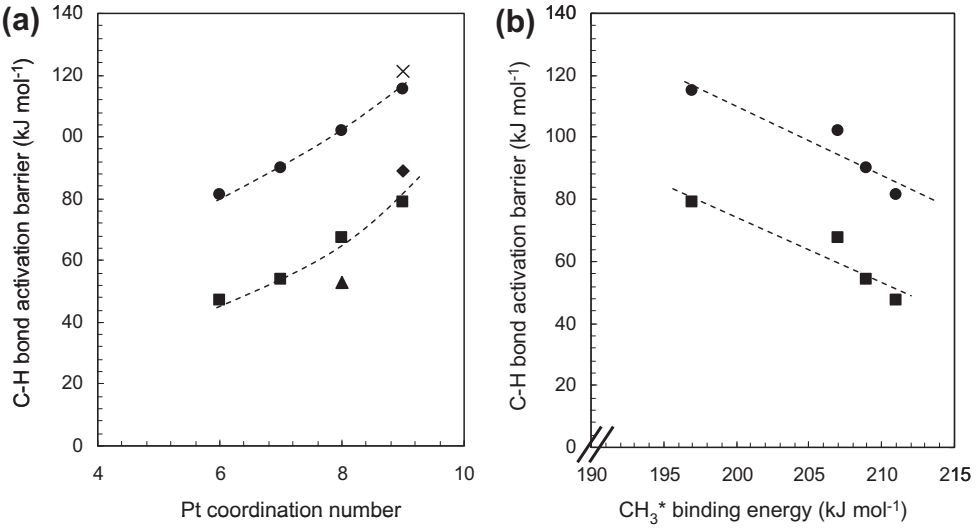

Fig. 6. (a) Effects of Pt coordination number on the DFT-calculated C–H bond activation barriers of CH_4 on Pt metal–metal (*–*) site pairs (■) and on Pt metal–oxygen atom (*–O*) site pairs (●) on the various Pt sites (type i = 1–4, Scheme 1) of a Pt_{201} cluster. C–H bond activation barriers on Pt metal–metal (*–*) site pairs at Pt(1 1 1) (♦) and Pt(1 0 0) (▲) surfaces and on Pt metal–oxygen atom (*–O*) site pairs at Pt(1 1 1) (×) surfaces are included for comparison. (b) Effects of CH_3* binding energy at the various Pt sites on the C–H bond activation barriers of CH_4 on Pt metal–metal (*–*) (■) and Pt metal–oxygen atom (*–O*) (●) site pairs on the surfaces of a Pt_{201} cluster. The data points correspond to sites 4, 3, 2, 1 (Scheme 1) with increasing CH_3* binding energy (see Table 4).

tion on Pt clusters was found to be slightly exothermic rather than endothermic. The small increase in reaction exothermicity is likely resulted from small perturbations in the Pt bond order on cluster surfaces caused by the presence of coordinatively unsaturated metal atoms located at the neighbor and next-nearest neighbor sites that increase the Pt–C interactions slightly.

The barriers for the C–H bond activation on *–* site pairs are correlated directly with the coordination number of the Pt atom that carries out the oxidative insertion step on both the (1 1 1) and (1 0 0) facets, as shown in Fig. 6a. The barriers for reactions carried out at the Pt terrace sites (79 kJ mol^{-1} for site 4, Scheme 1) are significantly higher than the more coordinatively unsaturated corner, edge, and (1 0 0) sites (sites 1, 2, and 3, respectively, in Scheme 1), as the terrace sites bind the CH_3* in the product state much more weakly than the coordinatively unsaturated sites. As the Pt coordination number decreases from 9 to 6, the C–H bond activation barriers decrease (from 79 to 47 kJ mol^{-1}, Fig. 6a) and the overall reaction becomes more exothermic as a result of the stronger CH_3* binding to the Pt site. Taken together with the nearly fully formed Pt–CH_3 bonds in the transition states (Pt–CH_3 = 0.222 nm at the transition state vs. Pt–CH_3 = 0.207 nm at the product state, Table A.2), the correlation between the C–H bond activation barriers and the Pt coordination numbers (also the reaction energies) suggests a direct relationship between the C–H bond activation barriers and the CH_3* binding energies (given by the heats of CH_3* adsorption in Table 4), as plotted in Fig. 6b. The barrier for the site giving a methyl binding energy of 207 kJ mol^{-1} is slightly higher than predicted from the linear correlation. This structure is the only one for which CH_3* groups reside at (1 0 0) surfaces, while all other points reflect events on (1 1 1) facets. Scatters are expected in such linear relationships upon changing the surface geometries involved in the binding because such a change leads to steps that are no longer belong to the same reaction family [43].

3.6. Theoretical assessment of the initial C–H bond dissociation in CH_4 and CO oxidation assisted by metal–oxygen site pairs on Pt_{201} clusters with a single chemisorbed oxygen atom

Next, we examine the C–H bond activation steps on the various *–O* site pairs (Step 5, Scheme 2), each of which is formed from a single chemisorbed O* atom and a vicinal * site on the Pt_{201} cluster. Surfaces of the model Pt_{201} cluster with a single O* atom resemble those encountered at low O_2/CH_4 ratios during CH_4–O_2 catalysis for which CO* intermediates are most likely to desorb and direct partial oxidation might become feasible. We first consider the O*

Table 3
Average Pt coordination numbers, heats of atomic oxygen adsorption, intrinsic and effective barriers for CO* and O* reactions on a cubo-octahedral Pt cluster (1.8 nm) consisting of 201 Pt atoms and on a Pt(1 1 1) extended surface.

Oxygen adsorption sites[a]	Average Pt coordination	Heat of O* adsorption, Q_O (kJ mol^{-1})	Intrinsic barrier for CO*–O* reactions, $(E_j)_{CO^*-O^*}$ (kJ mol^{-1})[c]	Effective barrier for CO*–O* reactions, $(E_j)_{CO^*-O^*,eff}$ (kJ mol^{-1})[d]
I	6.5	133	112	−72
II	7.3	114	88	−82
III	7.5	106	123	−69
IV	8.3	98	69	−92
V	9	96	82	−87
Pt(1 1 1) surface[b]	9	89	–	–

[a] Refer to Scheme 1 for the location of these sites.
[b] Single crystal Pt(1 1 1) surface.
[c] Calculated using Eq. (19).
[d] Calculated using Eq. (20), averaging over all plausible reaction paths by considering the various types of Pt sites vicinal of the O* atom.

binding energies at the various oxygen adsorption sites j (j = I–V, Scheme 1) and then analyze the effects of these binding strengths on the C–H bond activation barriers before extending the analysis to CO oxidation reactions.

The O* atoms preferentially reside at threefold fcc sites (labeled II, IV, V in Scheme 1b) on (1 1 1) surfaces and at bridge sites (labeled I and III in Scheme 1c) on (1 0 0) surfaces. The binding energies of isolated O* at these sites are reported as their respective heats of oxygen adsorption (Q_O, Eq. (2)) in Table 3. The heat of oxygen adsorption decreased from 133 to 96 kJ (mol O*)$^{-1}$ as the average coordination of the Pt atoms covalently bound to the O* increased from 6.5 to 9. At the fcc terrace sites on the (1 1 1) surfaces (site V, Scheme 1b) in which the average Pt coordination ($\langle CN \rangle$) approaches the value of 9, the heat of oxygen adsorption (96 kJ mol^{-1}) becomes similar to those on the extended Pt(1 1 1) surfaces (89 kJ mol^{-1}), which exhibit the same average coordination.

The presence of O* atoms near CH_4* species may assist C–H bond activation (Step 5) via concerted interactions reminiscent of the three- and four-centered transition states involved in oxidative addition [44], σ-bond metathesis [45], and oxidative hydrogen migration [46], implicated in ligand-assisted C–H bond activation that can occur in organometallic complexes [47]. Such O*-assisted C–H activation routes have also been proposed for CH_3OCH_3 [48], CH_4 [23], and C_2H_6 [27] oxidation on O*-covered Pt clusters. In the O*-assisted C–H bond activation step, a Pt atom inserts into and elongates the C–H bond as the CH_4 evolves into the $(H_3C^*–OH^*)^‡$ transition state complex (Fig. A.2, see Table A.3 for detailed bond length information), similar to the oxidative insertion step described previously on *–* site pairs (Section 3.5). The O* atom that is chemisorbed on the threefold fcc site (site II, IV, or V, Scheme 1) shifts to the bridge site directly across from the Pt atom that carries out the oxidative insertion as the reaction proceeds in order to interact with the H-atom in the C–H bond. The O* atom chemisorbed on the (1 0 0) surface (site I or III, Scheme 1) already resides at the bridge site vicinal to the CH_4* and thus is appropriately positioned to abstract the targeted H-atom. The O* and H interaction results in O–H bond lengths of 0.139–0.146 nm in the transition state (Table A.3). The C–H bond distance in the transition state was calculated to be 0.130–0.134 nm, which is 0.021–0.025 nm shorter than those found without the assistance of O* on *–* site pairs (C–H bond distance = 0.152 nm, Section 3.5).

The C–H bond activation barriers on the various *–O* site pairs, $(E_i)_{*-O^*}$, are estimated by the energy difference between the $(CH_3^*–OH^*)^‡$ transition state and the CH_4 in the gas phase. The barrier is reported for each type of Pt atom (i = 1–4, Scheme 1) in the *–O* site pairs, calculated by averaging the individual rate constants (each of which contains the individual barrier, $E_{C-H,i,j}$) of all plausible reaction paths at that site resulting from using the different vicinal O* atoms (j = I–V, Scheme 1) to abstract the H, according to the following equation:

$$(E_i)_{*-O^*} = -k_B T \ln \left(\frac{\sum_{j=1}^{5} n_j \exp\left(-\frac{E_{C-H,i,j}}{k_B T}\right)}{\sum_{j=1}^{5} (n_j)} \right)_i \quad (18)$$

where n_j is the number of vicinal O* atoms of type j (1 = I, 2 = II, 3 = III, 4 = IV, 5 = V) in Scheme 1. The C–H bond activation barrier increased monotonically from 81 kJ mol^{-1} to 115 kJ mol^{-1} as the coordination number of the Pt atom (*) in the *–O* site pairs increased from 6 to 9 on the Pt_{201} clusters (Fig. 6a), approaching the calculated value for the similar step on extended Pt(1 1 1) surfaces (122 kJ mol^{-1}, Pt coordination number of 9). This trend reflects a direct relation of C–H bond activation barriers on *–O* pairs with the extents of Pt–CH_3 interaction at the transition state and with the CH_3* binding strengths. Such a relation is similar to those found for C–H bond activation on *–* site pairs (Section 3.5; Fig. 6a) because both of the C–H bond activation steps (on *–O* and *–* site pairs, Steps 4 and 5) proceed via an oxidative insertion mechanism. The barriers for C–H bond activation on *–O* site pairs are also influenced by the extent of O–H interactions at the transition state, which is related to the O* reactivity and Pt–O bond strength. The correlation of the barriers with the Pt–O bond strength, however, is much weaker than with the Pt–CH_3 bond strength [23], as expected from the weak interactions between the O and H at the transition state (O–H bond length is 0.139–0.146 nm vs. 0.098 nm at the product state).

The calculated C–H bond activation barriers on *–O* site pairs are, however, significantly larger (81–115 kJ mol^{-1}, Step 5) than similar barriers on *–* site pairs (47–79 kJ mol^{-1}, Step 4) for each of the Pt sites (the specific * in the *–O* or *–* site pair that carries out the oxidation addition step), as also found on Pt(1 1 1) surfaces (122 kJ mol^{-1} vs. 89 kJ mol^{-1}) and included in Fig. 6a. These larger barriers are the result of repulsive interactions between the O* and H-atom in the C–H bond that increase the transition state energies. Both of the C–H bond activation routes are expected to exhibit similar pre-exponential factors and entropy losses for the formation of the respective transition states ($(H_3C^*–H^*)^‡$ or $(H_3C^*–OH^*)^‡$) from CH_4(g) reactants because of the similar extent of interactions between methyl groups and Pt sites in these transition states (the Pt–CH_3 bond lengths for a type 4 Pt site are 0.222–0.230 nm; Tables A.2 and A.3). Taken together with the much lower C–H bond activation barriers on the *–* than on the *–O* sites for all Pt sites (Fig. 6a), we conclude that C–H bond activation of CH_4 occurs predominantly on *–* site-pairs at the low O* coverages prevalent at the conditions used for rate measurements in Sections 3.3 and 3.4. O* insertion steps (into CH_x* or C*) are kinetically irrelevant because they occur later along the reaction path, except on a small fraction of coordinatively unsaturated Pt atoms that bind the CH_x* strongly and thus are occupied by CH_x* (Section 3.4). The kinetic irrelevance of O* insertion steps for the majority of the Pt sites is consistent with the increase in measured O* selectivity (S_{O^*}) with O_2/CO ratio (Eq. (12), Fig. 3).

We consider next the reactions of CO with a single O* atom chemisorbed at the various sites on the Pt_{201} cluster. At such low O* coverages, CO* intermediates that form are most likely to desorb before encountering a second O* atom and undergoing further oxidation to CO_2, thus partial oxidation may become feasible. The resulting CO, however, can re-adsorb and sequentially oxidize to CO_2. An O* atom at site j (j = I–V) can react with a CO* adsorbed at any of the vicinal atop sites (i = 1–4; see Fig. A.3 in Appendix (Supplementary material) for examples on plausible O* and CO* reaction paths). The reaction energy diagram, which shows the energies of the transition, intermediate, and product states with respect to the gas-phase reactant state, is given in Fig. 5b; the structural details for each of these states are provided in Fig. A.4 and Table A.4 in Appendix (Supplementary material). The calcu-

Table 4
Pt coordination numbers, heats of CH_3* and molecular CO* adsorption on a cubo-octahedral Pt cluster (1.8 nm) consisting of 201 Pt atoms and on the Pt(1 1 1) extended surface.

Pt sites[a]	Pt coordination number	Heat of CH_3* adsorption, $Q_{CH_3^*,i}$ (kJ mol^{-1})	Heat of molecular CO* adsorption, $Q_{CO,i}$ (kJ mol^{-1})[c]
1	6	211	198
2	7	209	189
3	8	207	166
4	9	197	161
Pt(1 1 1) surface[b]	9	–	150

[a] Refer to Scheme 1 for the location of these sites.
[b] Single crystal Pt(1 1 1) surface.
[c] Eq. (3).

lated heats of non-dissociative adsorption for CO* at the different Pt sites, $Q_{CO,i}$ (Eq. (3)), increased from 161 to 198 kJ mol^{-1} as the Pt surface atom coordination decreased from 9 to 6 (Table 4). The activation barrier for the CO* and O* reaction (Step 8), $(E_j)_{CO^*-O^*}$, was calculated and reported for each type of O* atom (j = I–V, Scheme 1) using an expression that averages the rate constants for the various reaction paths. The barrier is thus an average of the exponential terms, each of which contains the individual barrier depending on the identity of the neighboring CO* adsorption sites (type i = 1–4, Scheme 1):

$$(E_j)_{CO^*-O^*} = -k_B T \ln \left(\frac{\sum_{i=1}^{4} n_i \exp(-\frac{E_{CO-O,j,i}}{k_B T})}{\sum_{i=1}^{4}(n_i)} \right)_j \quad (19)$$

where $E_{CO-O,j,i}$ is the energy difference between the $(CO^*–O^*)^‡$ transition state and the chemisorbed CO* at the reactant state and n_i is the number of vicinal Pt atoms of type i (i = 1–4). These barriers, as shown in Table 3, were calculated to be between 69 and 123 kJ mol^{-1} depending on the specific O* atom used to oxidize CO*. The site-specific heats of CO adsorption were subsequently subtracted from the intrinsic CO oxidation barriers to determine the effective barriers for the CO*–O* reactions, $(E_j)_{CO^*-O^*,eff}$. The effective barriers were evaluated for each type of O* atom (type j = I–V) by averaging over the different barriers resulting from the reactions of the O* with vicinal CO* bound on different types of Pt sites (type i = 1–4, Scheme 1):

$$(E_j)_{CO^*-O^*,eff} = -k_B T \ln \left(\frac{\sum_{i=1}^{4} n_i \exp\left(-\frac{(E_{CO-O,j,i}-Q_{CO,i})}{k_B T}\right)}{\sum_{i=1}^{4}(n_i)} \right)_j \quad (20)$$

where $Q_{CO,i}$, $E_{CO-O,j,i}$, and n_i are defined above. The effective barriers for CO*–O* reactions are much less than zero (<−65 kJ mol^{-1}, Table 3) for all O* atoms because the intrinsic barriers for CO*–O* reactions (Fig. 5b and Table 3) are much smaller than the heats of CO adsorption (Table 4). The heats of CO adsorption are approximately equal to the CO* desorption barriers because CO adsorption steps are non-activated with barriers that are less than 5 kJ (mol CO)$^{-1}$ at all surface sites. The difference in barriers between the CO*–O* reaction and the CO* desorption provides an estimate of the ratio of CO* oxidation to CO* desorption rates. This rate ratio, derived by assuming similar activation entropy values for these steps, exceeds 2×10^4 for each type of O* atom. The much larger rates for the CO*–O* reactions than for the CO* desorption indicate that the initial CO adsorption step is essentially irreversible. CO oxidation, as a result, is limited by the irreversible CO adsorption (reverse of Step 7) where CO binds on a Pt site vicinal to an O* atom via the formation of a $(CO(g)–^*)^‡$ complex (structures in Appendix Fig. A.6 (Supplementary material)). In the $(CO(g)–^*)^‡$ complex, the C=O bond is slightly elongated (from 0.116 nm to 0.117 nm) and the Pt–CO bond (0.185 nm) is formed. The ensemble-averaged barrier for CO oxidation, calculated by averaging the CO adsorption barriers over all the *–O* site pairs on the Pt_{201} cluster, is less than 5 kJ (mol CO)$^{-1}$, which is within the errors associated with DFT calculations (<15 kJ (mol CO)$^{-1}$). Thus, the CO oxidation is considered as a non-activated step.

3.7. Comparison of experimentally measured and calculated ensemble-averaged oxygen selectivities in CH_4–O_2 mixtures

Fig. 7 shows the effects of temperature (885–935 K) on the ratio of rate constants for O_2 and C–H bond activation ($k_{O^*}K_{O_2}(3.5k_{[^*-^*]}K_{CH_4})^{-1}$) measured from $^{13}CH_4$–^{12}CO–O_2 reactions

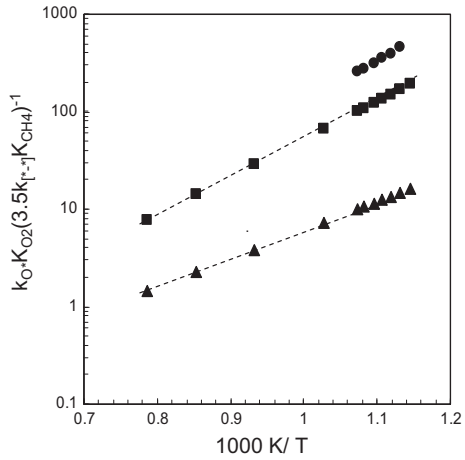

Fig. 7. Comparison of experimentally measured (●) and calculated (■, ▲) ratio of rate constants for O_2 and C–H bond activation ($k_{O^*}K_{O_2}(3.5k_{[^*-^*]}K_{CH_4})^{-1}$) on 1.8 nm (▲) and 33 nm (●, ■) Pt clusters. The experimental data (●) were measured in $^{13}CH_4$–^{12}CO–O_2 mixtures on 0.2 wt.% Pt/SiO_2 catalyst (0.3 mg cat., 33 nm average Pt cluster diameter, 0.022 kPa O_2, 0.16 kPa CO, 1.3 kPa $^{13}CH_4$; 2.08 cm^3 s^{-1}, λ = 200, χ = 4700). The calculated ensemble-averaged rate constant ratios (■: 33 nm Pt cluster; ▲: 1.8 nm Pt cluster) were the same for the cases of random and energy-weighted O* placements at each temperature.

on Pt/SiO_2 (0.2 wt.%; 33 nm mean cluster diameter). The rate constant ratios ($k_{O^*}K_{O_2}(3.5k_{[^*-^*]}K_{CH_4})^{-1}$), together with the O_2/CO ratios, determine O* selectivities (Eq. (12)) and, in turn, the intrinsic limits of the maximum CO yields for direct CH_4 and O_2 reactions. The rate constant ratios for O_2 to C–H bond activation were larger than 200 in the 885–930 K range and decreased with increasing temperature.

These rate constant ratios are interpreted using a transition state theory formalism and the thermodynamic properties of reactants and transition states for O_2 and C–H bond activation:

$$\frac{k_{O^*}K_{O_2}}{3.5k_{[^*-^*]}K_{CH_4}} = \frac{1}{3.5} \times \exp\left(\frac{\Delta S^*_{O_2} - \Delta S^*_{CH_4}}{k_B}\right) \exp\left(-\frac{(\Delta H^*_{O_2} - \Delta H^*_{CH_4})}{k_B T}\right) \quad (21)$$

$\Delta S^*_{O_2}$ (or $\Delta S^*_{CH_4}$) and $\Delta H^*_{O_2}$ (or $\Delta H^*_{CH_4}$) are the changes in entropy and enthalpy, respectively, required to form the $(O^*–O^*)^‡$ (or $(H_3C^*–H^*)^‡$) transition states from gaseous O_2 (or CH_4) reactants. Linear regression analyses on the data in Fig. 7 using Eq. (21) led to estimates for the $(\Delta S^*_{O_2} - \Delta S^*_{CH_4})$ and $(\Delta H^*_{O_2} - \Delta H^*_{CH_4})$ terms. The $(\Delta S^*_{O_2} - \Delta S^*_{CH_4})$ term was found to be −31 J (mol-K)$^{-1}$; $\Delta S^*_{CH_4}$ reflects the entropy loss of CH_4(g) upon formation of the $(H_3C^*–H^*)^‡$ transition state in the C–H bond activation step on *–* site pairs and was previously reported to be −99 J (mol-K)$^{-1}$ and −108 J (mol-K)$^{-1}$ for CH_4–CO_2 and CH_4–H_2O mixtures, respectively [24]. Substituting these values into the $(\Delta S^*_{O_2} - \Delta S^*_{CH_4})$ term of −31 J (mol-K)$^{-1}$ give, in turn, an O_2 activation entropy ($\Delta S^*_{O_2}$) of ~−130 J (mol-K)$^{-1}$, which is less negative than the value predicted for an immobile $(O^*–O^*)^‡$ transition state (−175 J (mol-K)$^{-1}$). The measured enthalpy difference for the O_2 and CH_4 reactants to form their respective transition states ($\Delta H^*_{O_2} - \Delta H^*_{CH_4}$), is −81 kJ mol^{-1}. This value, taken together with non-activated O_2 dissociation steps [23], gives a $\Delta H^*_{CH_4}$ value, which is used to approximate the C–H bond dissociation barrier on *–* site pairs (Step 4), of 81 kJ mol^{-1}, consistent with the measured barriers for this step during CH_4 decomposition (78 kJ mol^{-1}), CH_4–CO_2 (83 kJ mol^{-1}), and CH_4–H_2O (75 kJ mol^{-1}) reactions [24]. These measured barriers are compared with the ensemble-averaged barrier (E_{CH_4}), which is related to the calculated CH_4 reaction rate constant (k_{CH_4}), derived from DFT estimates of C–H bond activation

barriers at various Pt sites i ($E_{C-H,i}$, $i = 1–4$, Scheme 1, Fig. 6a) weighed by their relative abundances on Pt_{201} clusters (P_i):

$$k_{CH_4} = A \exp\left(\frac{-E_{CH_4}}{k_B T}\right) = \sum_{i=1-4} \left(A_{i,CH_4} \exp\frac{(-E_{C-H,i})}{k_B, T}\right) P_i \quad (22)$$

A is the ensemble-averaged pre-exponential factor and $(A_i)_{CH_4}$ is the pre-exponential factor for each Pt site (i). Assuming that $(A_i)_{CH_4}$ values for all Pt sites remain the same, Eq. (22) can be rearranged to give the ensemble-averaged barrier for C–H bond activation on *–* site-pairs (E_{CH_4}):

$$E_{CH_4} = -k_B T \ln\left(\sum_{i=1-4} P_i \exp\frac{(-E_{C-H,i})}{k_B T}\right) \quad (23)$$

E_{CH_4} was calculated to be 76 kJ mol^{-1} for 33 nm Pt clusters, consistent with measured values (81 kJ mol^{-1}).

The ensemble-averaged rate constant ratios for 1.8 nm and 33 nm cubo-octahedral Pt clusters were obtained from measured differences in O_2 and C–H activation entropies ($\Delta S^*_{O_2} - \Delta S^*_{CH_4} = 31$ J (mol-K)$^{-1}$), DFT-derived C–H bond activation barriers on the various Pt sites ($E_{C-H,i}$, Fig. 6a and b) and their relative abundances (P_i), assuming that O_2 dissociation is barrierless ($E_{O_2} < 3$ kJ mol^{-1} [23]) and that activation entropies are independent of the specific activation site ($\Delta S^*_{O_2} - \Delta S^*_{CH_4}$):

$$\frac{k_{O^*} K_{O_2}}{3.5 k_{[^*-^*]} K_{CH_4}} = \frac{1}{3.5} \exp\left(\frac{\Delta S^*_{O_2} - \Delta S^*_{CH_4}}{k_B}\right) \frac{\exp\left(\frac{-E_{O_2}}{k_B T}\right)}{\sum_{i=1-4} P_i \exp\left(\frac{-E_{C-H,i}}{k_B T}\right)} \quad (24)$$

The specific location of O* (random or energy-weighted, Eq. (5)) did not influence ensemble-averaged rate constant ratios, because rate constants for O_2 dissociation ($k_{O^*} K_{O_2}$) and C–H bond activation ($k_{[^*-^*]} K_{CH_4}$) were insensitive to O* binding energies. O_2 dissociation rate constants depend only on entropy losses and are therefore insensitive to O* location and surface coordination. C–H bond dissociation rate constants depend on the activation entropy and enthalpy for the formation of $(H_3C^*–H^*)^‡$ transition states from CH_4(g). The $(H_3C^*–H^*)^‡$ species do not involve O* (Sections 3.4–3.6) and, as a result, C–H activation rate constants also depend neither on the O* location nor binding energy. The ensemble-averaged rate constant ratios for O_2 and C–H bond activation ($k_{O^*} K_{O_2} (3.5 k_{[^*-^*]} K_{CH_4})^{-1}$) were much larger than unity at all temperatures relevant to the practice of catalytic CH_4–O_2 reactions (873–1273 K, Fig. 7) for the large Pt clusters (33 nm mean cluster size). The ratios were smaller and approached unity at higher temperatures (>1300 K) for the small Pt clusters (1.8 nm mean cluster size), indicating that desorbed CO may become detectable in effluent streams but at temperatures unlikely to preserve their small size.

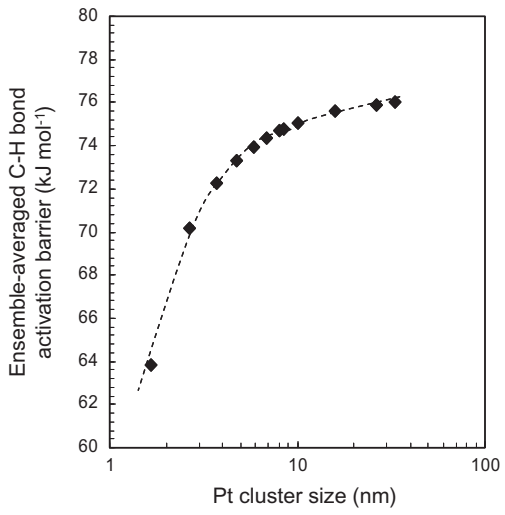

Fig. 8. Effects of Pt cluster size on the calculated ensemble-averaged C–H bond activation barriers of CH_4 on Pt metal atom (*–*) site pairs using Eq. (23).

Pt surface coordination and cluster size influence ensemble-averaged rate constant ratios $\{k_{O^*} K_{O_2} (3.5 k_{[^*-^*]} K_{CH_4})^{-1}\}$, predominantly because of their concomitant effects on the C–H bond activation rate constants ($k_{[^*-^*]} K_{CH_4}$), since they do not affect the O_2 dissociation rate constants ($k_{O^*} K_{O_2}$) [23]. The ensemble-averaged C–H bond activation barriers calculated using Eq. (23) decreased from 76 kJ mol^{-1} to 64 kJ mol^{-1} (Fig. 8) as Pt clusters became smaller (33–1.8 nm) and as the surface fraction of coordinatively unsaturated metal atoms concomitantly increased. This decrease in barriers with cluster size leads to an increase in the ensemble-averaged CH_4 reaction rate constants (Eq. (22)) and, in turn, to a decrease in the calculated ensemble-averaged rate constant ratios (Fig. 7) and smaller measured O* selectivities (Fig. 3) on the smaller clusters.

O* selectivities (Eq. (12)), determined from ensemble-averaged rate constant ratios $\{k_{O^*} K_{O_2} (3.5 k_{[^*-^*]} K_{CH_4})^{-1}\}$ and O_2/CO ratios, were used in a kinetic model that captures the CH_4 oxidation to CO (and H_2) and their sequential oxidation to estimate the intrinsic limits of the maximum CO yields. Solving the mole balances for CH_4, CO, and O_2 in an isothermal–isobaric plug-flow reactor gives the maximum CO yields (Fig. A.7 in Appendix (Supplementary material)) as a single-valued function of O* selectivities. These results suggest that a small amount of CO, initially formed in the reactor, would undergo rapid sequential oxidation because of the high $k_{O^*} K_{O_2} (3.5 k_{[^*-^*]} K_{CH_4})^{-1}$ values and low O_2/CO ratios.

CO/CO_2 ratios were much lower on Rh than on Pt clusters at all conditions before the complete consumption of limiting O_2 reactants (Fig. 2a and b), suggesting that CO oxidation reactions are more effective on Rh clusters. We were unable to measure the O* selectivities in $^{13}CH_4$–CO–O_2 mixtures on Rh clusters at all O_2/CO ratios without completely depleting the limiting reactants, which could be CO or O_2 depending on the O_2/CO ratio, because of the high CO oxidation rates. These results suggest more reactive surfaces for CO oxidation and, in turn, higher O* selectivities toward CO on Rh than on Pt, apparently caused by the stronger binding of O* on Rh (DFT-calculated O* binding strengths are 469 kJ mol^{-1} and 354 kJ mol^{-1} for a single O* chemisorbed on Rh(1 1 1) and Pt(1 1 1), respectively [49]), and the concomitantly larger O* contents on Rh cluster surfaces. Catalytic effects of oxygen vacancies, which have shown to increase the C–H bond activation rates, were not detected at any amount of measurable O_2 and O_2/CH_4 ratio on Rh clusters. The C–H bond activation rate constants on Rh instead increase solely with oxygen chemical potential, throughout the entire O_2/CH_4 range (0.02–200; 873 K) [50]. The bulk of the Rh clusters, as predicted from the phase equilibrium thermodynamics of Rh and their oxides (Rh_2O_3, RhO_2), remains in the oxide phase even at an equilibrium O_2 pressure of 0.01 kPa at 873 K [51]. In CH_4–O_2 mixtures, the Rh clusters are likely in their oxide phases in the presence of O_2 and surface oxygen atoms on the Rh oxide clusters appear to selectively promote the CO oxidation, leading to the lower CO/CO_2 ratios on Rh than on Pt. The low maximum CO yields on Pt and the expected even lower yields on Rh led us to conclude that direct CO (and H_2) formation from CH_4 and O_2 reactions is unlikely at CH_4 conversions of practical interest on both the Pt and Rh clusters, because these products are much more reactive than CH_4. These partial oxidation products are formed from sequential reactions of CO_2 and H_2O with residual CH_4 at all practical temperatures and O_2/CH_4 ratios.

4. Conclusion

CO/CO_2 ratios resulting from CH_4 and O_2 reactions on supported Pt and Rh clusters were measured by varying the residence time and O_2/CH_4 feed ratio independently in a regime of strict kinetic

control, achieved by extensive dilutions of catalyst pellets and the reactor bed. A small amount of CO was detected ($CO/CO_2 < 0.02$) only at very low O_2/CH_4 ratios ($O_2/CH_4 < 0.004$) as catalyst surfaces were depleted of reactive oxygen intermediates.

Oxygen selectivities, defined by the ratios of reactive collision probability (also the effective rate constant) of desorbed CO and CH_4 reactant, determine the CO/CO_2 ratios in CH_4–O_2 reactions. We have interpreted the oxygen selectivities rigorously in terms of elementary rate and equilibrium constants and measured their values by competitive $^{13}CH_4$ and ^{12}CO oxidation in $^{13}CH_4$–^{12}CO–O_2 mixtures. Reactive collision probabilities of CO with O^* on uncovered Pt clusters are much larger than those of CH_4. The higher reactivity for CO than CH_4 toward the O^* limits the maximum attainable CO yield from direct CH_4 and O_2 reactions.

Density functional theory (DFT) results are used within the framework of transition state theory and ensemble-averaging methods to calculate the oxygen selectivities. DFT calculations were carried out on the corner, edge, and terrace sites of a model cubo-octahedral Pt cluster (1.8 nm diameter) to probe the kinetically relevant steps and the identity of active sites involved in CH_4 and CO oxidation. CH_4 oxidation proceeds via kinetically relevant C–H bond dissociation over Pt atom site pairs (*–*) in which one of the Pt sites undergoes an oxidative insertion step into the C–H bond. The barriers for this step are correlated to the Pt–CH_3 bond strength and coordination number of the Pt atom that carries out the oxidative insertion step. CO oxidation proceeds via a non-activated molecular CO adsorption step; this step is irreversible because of the much larger barrier for its reverse step (CO^* desorption) than for the sequential CO^* and O^* recombination. The barriers for CO and CH_4 oxidation were calculated from ensemble averaging the individual barriers for the various types of surface sites on the model Pt cluster. These barriers, together with the measured activation entropies, give the calculated ensemble-averaged O^* selectivities. The O^* selectivities are proportional to O_2/CO ratios and are estimated to be much larger than unity, especially when a small amount of CO is formed initially, over the entire temperature range typical for CH_4–O_2 catalysis. These results unequivocally show that oxidation of CO intermediate is much more rapid than the activation of CH_4 reactant. The marked reactivity differences between CO and CH_4 lead to low intrinsic limits of the maximum CO yields from direct CH_4 and O_2 reactions at any practical extent of CH_4 conversion.

Acknowledgments

This study was supported by BP as part of the Methane Conversion Cooperative Research Program. We also gratefully acknowledge the computational support from the Molecular Science Computing Facility (MSCF) in the William R. Wiley Environmental Molecular Sciences Laboratory, a national scientific user facility sponsored by the US Department of Energy's Office of Biological and Environmental Research and located at the Pacific Northwest National Laboratory. Pacific Northwest is operated by Battelle for the Department of Energy.

Appendix A. Supplementary material

Supplementary data associated with this article can be found, in the online version, at doi:10.1016/j.jcat.2011.06.011.

References

[1] J.R. Rostrup-Nielsen, Catal. Today 71 (2002) 243.
[2] N. Dave, G.A. Foulds, Ind. Eng. Chem. Res. 34 (1995) 1037.
[3] D.A. Hickman, L.D. Schmidt, Science 259 (1993) 243.
[4] D.A. Hickman, E.A. Haupfear, L.D. Schmidt, Catal. Lett. 17 (1993) 223.
[5] D. Dissanayake, M.P. Rosynek, K.C.C. Kharas, J.H. Lunsford, J. Catal. 132 (1991) 117.
[6] W.J.M. Vermeiren, E. Blomsma, P.A. Jacobs, Catal. Today 13 (1992) 427.
[7] I. Tavazzi, M. Maestri, A. Beretta, G. Groppi, E. Tronconi, P. Forzatti, AIChE J. 52 (2006) 3234.
[8] A. Beretta, G. Groppi, M. Lualdi, I. Tavazzi, P. Forzatti, Ind. Eng. Chem. Res. 48 (2009) 3825.
[9] R. Horn, K.A. Williams, N.J. Degenstein, A. Bitsch-Larsen, D. Dalle Nogare, S.A. Tupy, L.D. Schmidt, J. Catal. 249 (2007) 380.
[10] B.C. Enger, R. Lødeng, A. Holmen, Appl. Catal. A 364 (2009) 15.
[11] M.A. Vannice, J.E. Benson, M. Boudart, J. Catal. 16 (1970) 348.
[12] R.L. David, Handbook of Chemistry and Physics, 87th ed., CRC Press, Boca Raton, FL, 2006. p. 4–26, p. 4–30.
[13] R. Van Hardeveld, F. Hartog, Surf. Sci. 15 (1969) 189.
[14] J.P. Perdew, J.A. Chevary, S.H. Vosko, K.A. Jackson, M.R. Pederson, D.J. Singh, C. Fiolhais, Phys. Rev. B 46 (1992) 6671.
[15] G. Kresse, J. Hafner, Phys. Rev. B 49 (1994) 14251.
[16] G. Kresse, J. Furthmuller, Comput. Mater. Sci. 6 (1996) 15.
[17] G. Kresse, J. Furthmuller, Phys. Rev. B 54 (1996) 11169.
[18] D. Vanderbilt, Phys. Rev. B 41 (1990) 7892.
[19] H.J. Monkhorst, J.D. Pack, Phys. Rev. B 13 (1976) 5188.
[20] G. Henkelman, H. Jonsson, J. Chem. Phys. 113 (2000) 9978.
[21] R.M. Koros, E.J. Nowak, Chem. Eng. Sci. 22 (1967) 470.
[22] R. Madon, M. Boudart, Ind. Eng. Chem. Fund. 21 (1982) 438.
[23] Y.-H. Chin, C. Buda, M. Neurock, E. Iglesia, J. Am. Chem. Soc., in press.
[24] J. Wei, E. Iglesia, J. Phys. Chem. B 108 (2004) 4094.
[25] Estimated based on monolith volume of 2.5 cm^3, 66.7 cm ^{3} s^{-1} CH_4/air feed mixtures with an O_2/CH_4 ratio of 2, and 50% CH_4 conversion.
[26] A. Eichler, J. Hafner, Phys. Rev. Lett. 79 (1997) 4481.
[27] M. García-Diéguez, Y.-H. Chin, E. Iglesia, J. Catal., submitted for publication.
[28] The exact v_1 and v_2 values affect only the stoichiometry that appears in the S_{O^*} expression but not the functional dependence of S_{O^*} on O_2/CO ratios.
[29] J. Wei, E. Iglesia, J. Catal. 225 (2004) 116.
[30] J. Wei, E. Iglesia, J. Phys. Chem. B 108 (2004) 7253.
[31] A. Yamaguchi, E. Iglesia, J. Catal. 274 (2010) 52.
[32] H. Burghgraef, A.P.J. Jansen, R.A. van Santen, Surf. Sci. 324 (1995) 345.
[33] I.M. Ciobica, F. Frechard, R.A. van Santen, A.W. Kleyn, J.A. Hafner, J. Phys. Chem. B. 104 (2000) 3364.
[34] G. Jones, J.G. Jakobsen, S.S. Shim, J. Kleis, M.P. Andersson, J. Rossmeisl, F. Abild-Pedersen, T. Bligaard, S. Helveg, B. Hinnemann, J.R. Rostrup-Nielsen, I. Chorkendorff, J. Sehested, J.K. Norskov, J. Catal. 249 (2008) 147.
[35] N.N. Greenwood, A. Earnshaw, Chemistry of the Elements, second ed., Butterworth-Heinemann, 1997. p. 1148.
[36] S.I. Sanchez, L.D. Menard, A. Bram, J.H. Kang, M.W. Small, R.G. Nuzzo, A.I. Frenkel, J. Am. Chem. Soc. 131 (2009) 7040.
[37] C. Buda, M. Neurock, unpublished results.
[38] Y. Zhao, D.G. Truhlar, Theor. Chem. Acc. 120 (2008) 215.
[39] G. Scuseria, V.N. Staroverov, in: C.E. Dykstra, G. Frenking, K.S. Kim, G.E. Scuseria (Eds.), Theory and Applications of Computational Chemistry: The First 40 Years, Elsevier, Amsterdam, The Netherlands, 2005, p. 669.
[40] S. Sakaki, M. Ieki, J. Am. Chem. Soc. 115 (1993) 2373.
[41] P.S. Venkataraman, M. Neurock, V.S. Lusvardi, J.J. Lerou, D.D. Kragten, R.A. van Santen, J. Phys. Chem. B 106 (2002) 1656.
[42] M. Neurock, Appl. Catal. 160 (1996) 169.
[43] R.A. van Santen, M. Neurock, S.G. Shetty, Chem. Rev. 110 (2010) 2005.
[44] W.D. Jones, Acc. Chem. Res. 36 (2003) 140.
[45] T.R. Cundari, J. Am. Chem. Soc. 116 (1994) 340.
[46] J. Oxgaard, R.P. Muller, W.A. Goddard III, R.A. Periana, J. Am. Chem. Soc. 126 (2004) 352.
[47] T.R. Cundari, T.V. Grimes, T.B. Gunnoe, J. Am. Chem. Soc. 129 (2007) 13172.
[48] A. Ishikawa, M. Neurock, E. Iglesia, J. Am. Chem. Soc. 129 (2007) 13201.
[49] R.A. van Santen, M. Neurock, Molecular Heterogeneous Catalysis: A Conceptual and Computational Approach, Wiley-VCH, Weinheim, Cambridge, 2006.
[50] Y.-H. Chin, E. Iglesia, unpublished results.
[51] O. Muller, R. Roy, J. Less-Common Metals 16 (1968) 129.
[52] The O^* coverages during steady-state catalysis depends on the operating O_2/CH_4 ratios, the rate and thermodynamic constants for the O_2 and C–H bond activation elementary steps, which vary with Pt cluster size. For the 33 nm Pt clusters, the surfaces are depleted of O^* for O_2/CH_4 ratios below 0.08 at 873 K.